

Photoexcitations in a 1D manganite model: From quasiclassical light absorption to quasiparticle relaxations

Thomas Köhler,¹ Sangeeta Rajpurohit,² Ole Schumann,¹ Fabian R. A. Biebl,¹ Mohsen Sotoudeh,² Stephan C. Kramer,¹ Peter E. Blöchl,^{2,1} Stefan Kehrein,¹ and Salvatore R. Manmana¹

¹*Institut für Theoretische Physik, Georg-August-Universität Göttingen, 37077 Göttingen, Germany*

²*Institut für Theoretische Physik, TU Clausthal, 38678 Clausthal-Zellerfeld, Germany*

(Dated: October 25, 2016)

We investigate the behavior of 1D correlated systems following a photo-excitation by combining ab-initio methods, time-dependent matrix product state (MPS) approaches, analytical insights from quantum Boltzmann equations, and molecular dynamics (MD) simulations to describe the dynamics on different time scales ranging from femtoseconds up to nanoseconds. This is done for manganite systems in the material class $\text{Pr}_{1-x}\text{Ca}_x\text{MnO}_3$. We derive one-dimensional ab-initio model Hamiltonians for which we compute the ground states at different values of the doping using MD simulations. At half doping, we obtain a magnetic microstructure of alternating dimers which we use as a starting point to formulate a one-dimensional Hubbard-type model. In this strongly correlated 1D system we address the formation of quasiparticles after photoexcitations. We introduce a quasiclassical model for the absorption process of light which takes into account the backaction of the electrons to the electromagnetic field and compare the results with the ones obtained with a Peierls substitution ansatz in which we neglect the backaction. Taking this effect into account leads to a stronger response since the emitted radiation can be re-absorbed by neighboring particles. We use the resulting state as starting point for the short-time dynamics which we obtain from 'numerically exact' MPS calculations. The dynamics is analyzed concerning the formation and lifetime of quasiparticles which form a starting point for the description of the relaxation process via a linearized quantum Boltzmann equation. In this way, our work constitutes a first step to building a unifying theoretical framework for the description of photoexcitations in strongly correlated materials over a wide range of time scales, capable of making predictions for ongoing experiments investigating pump-probe situations and unconventional photovoltaics.

I. INTRODUCTION

The optical excitation of matter and its subsequent dynamics is an intriguing phenomenon which reveals a whole range of interesting physical effects. In the presence of strong correlations, this topic is one of ongoing experimental¹⁻⁶ and theoretical studies,⁷⁻¹⁰ and a detailed understanding of these processes is believed to open up new pathways for technological applications. For example, the controlled application of pump-probe setups on the femtosecond time scale in recent experiments has lead to a number of interesting discoveries, like the formation of metastable states, some of which are superconducting.¹¹ Light irradiation of interfaces of correlated materials has shown the possibility to realize unconventional photovoltaic effects¹²⁻¹⁸ not based on the formation of excitons, but rather of polarons, i.e., quasiparticles consisting of electrons and phonons which are formed or excited due to the light absorption. These phenomena span a wide range of timescales: the absorption process of light can last as little as femtoseconds in pump-probe experiments, while the subsequent relaxation process can last up to the order of nanoseconds, with phonon effects kicking in on typical time scales of the order of picoseconds.^{19,20} From a theoretical point of view, it is a major challenge to find a unifying description of the evolution of these excitations, in particular in the presence of strong correlations.

Here, we attempt to gain insights into the full process starting from the photoexcitation itself up to the relax-

ation of the emerging quasiparticles by combining a variety of theoretical approaches. To be more specific, the scope of this paper is fourfold. First, we formulate ab-initio model systems for manganites whose ground states we obtain using MD simulations. Based on these results, we identify one-dimensional structures for which we propose a viable path towards a coherent description of the quantum-mechanical processes in the dynamics following the excitation which occur on a large span of time scales. For this, we develop a suitable combination of different theoretical methods. Third, we model the excitation process itself by a semiclassical approach which includes back-action effects, in contrast to approaches often used in the literature like the Peierls substitution²¹⁻²⁵ or the creation of local excitations as doublons or holon-doublon pairs^{7,26-29} in which the backaction is neglected. With this, as the fourth scope of the paper, we explore the role of correlations and magnetic microstructures in the dynamics of excited manganite systems. We find that the presence of strong magnetic microstructures can significantly enhance the lifetime of the excitations.

Let us describe in more detail our approach for tackling the huge span of time scales as illustrated in Fig. 1: We start with a three-dimensional ab-initio model for the electronic structure of $\text{Pr}_{1-x}\text{Ca}_x\text{MnO}_3$.^{30,31} From this we derive a simpler one-dimensional MD model which yields the magnetic order of the t_{2g} spins as a function of the doping. We further simplify our description by using the obtained magnetic order as an effective external field in the Hubbard model, which we here use as

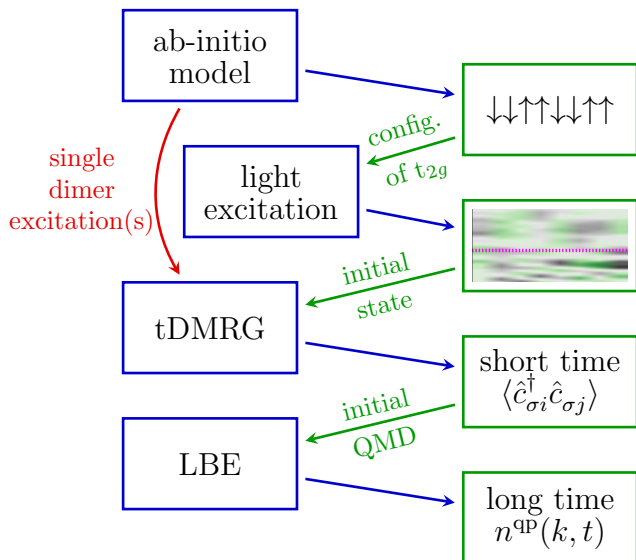


FIG. 1: Sketch of the work flow used in this paper: we develop a model description for a 1D manganite using ab-initio approaches, showing that the system at half doping has a dimerized magnetic micro-structure due to the behavior of the t_{2g} electrons. This is used for modelling the photoexcitation first in a semiclassical way, but also by a many-body Hamiltonian in which the excitations are described by shifting electrons on the sites. These initial states are treated with tDMRG to obtain local densities and the momentum distribution functions. From this, the quasiparticle momentum distribution (QMD) function of the excitation is obtained, and using a linearized Boltzmann equation (LBE), the relaxation time scales are estimated.

minimal model for interacting electrons in a solid. For the case $x = 0.5$, we introduce a mean-field approach based on the Klein-Gordon equation to study the photoexcitation process of the e_g electrons. Often, the back-action of the electrons to the electromagnetic field is neglected.^{7,22–29,32} In contrast, our approach allows to take into account the back-action of the electronic system to the light field, as discussed in Sec. II.3 in detail, however without the need of fully quantizing the light field. This would be possible in principle, e.g. with extensions of the adaptive time-dependent density matrix renormalization group (tDMRG)^{33–37} to treat dissipative systems,³⁸ but is beyond the scope of this paper and is left for future investigations.

The result of this mean-field type simulation of the excitation process is then used as initial condition for a simulation which takes into account all correlations. For this we apply the tDMRG in its matrix product states³⁹ (MPS) formulation. The time integration is performed using the variational ansatz of Refs. 40 and 41. As discussed in III.2.1, an approximate description for the initial state obtained by the semiclassical excitation is to shift an electron on every other site. This can be directly implemented in the tDMRG, allowing us to treat larger

systems. An interesting aspect is the possible formation of quasi-particles as seen in Ref. 42. Here, we address this by analyzing the quasi-particle content in the momentum distribution function (MDF) of the system out-of-equilibrium obtained by the tDMRG. These tDMRG simulations reveal the short-time dynamics since their accuracy goes down in the course of the time evolution as entanglement is increasing.³⁵ Therefore, to capture the long-time behavior, we use a quantum Boltzmann-equation⁴³ (QBE) and determine from a linearized ansatz the relaxation rates of the quasi-particle momentum distribution. In this combination, we are able to make predictions over the several orders of magnitudes of time scales involved, with each method working best in a certain time window of this dynamical process.

The manganite systems we are treating here are particularly interesting since they are prototypical for materials with strongly correlated electrons, phonons and spin excitations and host a rich phenomenology.⁴⁴ Many of these materials exhibit the Jahn-Teller (JT) effect that distorts the local environment of the central metal ion because of the occupation of a particular orbital type. It leads to long-range cooperative distortions and orbital ordering especially in cuprates and manganites with perovskite structure.

Such perovskite manganites can be broadly classified according to the widths of their e_g -like bands that are partially filled⁴⁴. The e_g orbitals couple to the lattice via the cooperative JT effect and via super-exchange interactions to the electronic spin. In such systems orbital-ordering phase transitions can occur at which the magnetic susceptibility and phonon properties will be affected simultaneously. The possibility to control the electron-phonon coupling in perovskite manganites by proper doping makes these materials interesting candidates for functional devices. Originally, the pervasive interest in these materials was sparked by the phenomenon of colossal magneto-resistance in manganites⁴⁵. More recently, multilayer manganites, as well as titanates, are considered as potential systems for unconventional realizations of the photo-voltaic effect which might lead to next-generation applications^{12–18}. In this realm, a promising perovskite material is the aforementioned $\text{Pr}_{1-x}\text{Ca}_x\text{MnO}_3$ with a doping parameter $x \in [0, 1]$. Around intermediate doping, $x \approx 0.5$, it shows charge ordering, a prototypical behavior for the low bandwidth case. Special cases of interest are $x = 0$ (PrMnO_3), $x = 1$ (CaMnO_3), and $x = 0.5$ ($\text{Pr}_{0.5}\text{Ca}_{0.5}\text{MnO}_3$ subsequently abbreviated as PCMO). The doping allows for a control of the electron-phonon coupling.

In these systems, a characteristic so-called CE-type⁴⁶ magnetic structure is encountered which can be described as one-dimensional zig-zag chains of ferromagnetic order and which mutually experience an anti-ferromagnetic coupling between neighboring zig-zag chains. In this way, the e_g orbitals pointing along the chain form a conduction channel. As a consequence, the electronic properties of these chains are similar to purely one-dimensional systems, so that inspired by this observation in the following

we will think of the situation as a quasi-1D correlated system which we are going to model by a one-dimensional Hubbard Hamiltonian. In this model system for PCMO we will investigate the dynamics and relaxation behavior of photo-excitations as described above.

This is particularly interesting, because at the moment it is unclear how the interplay of the chemical composition and the electron-phonon coupling influence the dynamics following photo-excitations, notably also their importance for the life-times of the quasi-particles emerging in the dynamics. The magnitudes of the life-times, however, is an important point since it determines whether the absorbed energy can actually be harvested.

The paper is organized as follows. In Secs. II.1 and II.2, we introduce our ab-initio 1D manganite model and the strongly correlated Hubbard-type Hamiltonian which is used for treating the photoexcitation dynamics. In Secs. II.3 we introduce our semiclassical treatment of the photoexcitation which includes the backaction of the electrons to the light-field, and in Sec. II.4 we discuss further approaches relevant for our work. Sec. II.5 presents details of the tDMRG calculations performed. In Secs. II.6 and II.7 we discuss the quasiparticle content in the momentum distribution functions, and our linearized Boltzmann equation approach for estimating the lifetimes of the excitations. Our results are presented in Sec. III: Sec. III.1 discusses the ground states of the 1D manganite model obtained by molecular dynamics simulations at different fillings. In Sec. III.2 the results of the photoexcitations treated by the semiclassical approach of Sec. II.3 are compared to the ones obtained with the Peierls-substitution of Sec. II.4.2. In Sec. III.3 our tDMRG results for the dynamics following the different types of photoexcitations are analyzed. This is complemented by the results for the momentum and quasiparticle distribution functions discussed in Sec. III.4. In Sec. III.5 we present our results for the relaxation rates obtained from the linearized Boltzmann equation ansatz. In Sec. IV we summarize. The considerations of Sec. II.2 are complemented by Appendix A.

II. MODELS AND METHODS

In this section we are going to derive an effective strongly correlated 1D model for PCMO motivated by the observation of one-dimensional features like the CE-structures in manganites. As shown in the following, it takes the shape of a Hubbard chain at quarter filling with pairwise alternating external magnetic fields. While we mainly focus our investigation for values of the parameters of this model as close as possible to the PCMO situation, tuning the parameters allows us to identify and theoretically explore the behavior of the photo-excitation in different regimes.

II.1. Tight-binding model for manganites

The physics of manganites is characterized by strong correlations of electrons, phonons and classical spins. The electrons are those in the two e_g orbitals of the Mn ions. The three low-lying spin-aligned electrons in the t_{2g} states of the Mn-ions can be described as classical spins. The two Jahn-Teller active distortions of the MnO_6 octahedra are the relevant phonons, which are strongly coupled to the electrons. All other degrees of freedom are either absorbed into the dynamical variables of the model, or they are considered as a bath and not treated explicitly. In order to cope with the complexity of manganites, however, one resorts to simpler model descriptions.⁴⁷

The three-dimensional model and its parameterization via first-principles calculations is described elsewhere³¹. The three-dimensional model is further simplified to obtain a one-dimensional model described in the following.

The total energy functional of density-functional theory^{48,49} is replaced by the potential energy of the model which takes the form

$$E_{\text{pot}} = E_e + E_S + E_{ph} + E_{e-ph} + E_{e-S}, \quad (1)$$

where E_e is the energy of the isolated electronic subsystem, E_S describes the antiferromagnetic interaction of the t_{2g} orbitals on neighboring Mn-sites, and E_{ph} is the energy of the Jahn-Teller active phonons. The electronic energy $E_e = E_{kin} + E_U$ consists of the kinetic energy E_{kin} and the electron-electron interaction E_U . The remaining two terms describe the electron-phonon coupling E_{e-ph} , due to the Jahn-Teller interaction, and the Hund's coupling E_{e-S} between electrons in the e_g and t_{2g} shells of a given Mn-site.

The e_g electrons are described, in the spirit of density-functional theory by one-particle wave functions. The one-particle wave function with band index n is expressed as

$$|\psi_n\rangle = \sum_{\sigma, \alpha, R} |\chi_{\sigma, \alpha, R}\rangle \psi_{\sigma, \alpha, R, n} \quad (2)$$

in terms of local spin-orbitals $|\chi_{\sigma, \alpha, R}\rangle$ having spin $\sigma \in \{\uparrow, \downarrow\}$, spatial orbital character α denoting the $d_{x^2-y^2}$ for $\alpha = a$ and $d_{3z^2-r^2}$ for $\alpha = b$ orbitals. The orbital is centered at the Mn-site specified by the index R .

In the one-dimensional model, only the d-orbital pointing along the chain can participate in the hopping. Due to symmetry, the other orbital with δ symmetry cannot interact with the oxygen p-orbital from which the d-d hopping is derived. Thus, for the one-dimensional system, the kinetic energy of the e_g electrons is

$$E_{kin} = -t_{hop} \sum_n f_n \sum_{\sigma} \sum_R \sum_{D \in \{\pm 1\}} \psi_{\sigma, b, R, n}^* \psi_{\sigma, b, R+D, n} \quad (3)$$

We omitted a constant energy term and a constant energy shift.

The onsite Coulomb energy E_U between the e_g electrons can be expressed by the one-particle reduced den-

sity matrix,

$$\rho_{\sigma,\alpha,\sigma',\beta,R} = \sum_n f_n \psi_{\sigma,\alpha,R,n}^* \psi_{\sigma',\beta,R,n}. \quad (4)$$

It can be broken up as

$$E_U = E_H + E_{SIC} + E_{OR} \quad (5)$$

into the Hartree energy

$$E_H = \frac{1}{2}(U - 3J_{xc}) \sum_R \left(\sum_{\sigma,\alpha} \rho_{\sigma,\alpha,\sigma,\alpha,R} \right)^2 \quad (6)$$

and a self-interaction correction

$$E_{SIC} = -\frac{1}{2}(U - 3J_{xc}) \sum_R \sum_{\sigma,\sigma',\alpha,\beta} |\rho_{\sigma,\alpha,\sigma',\beta,R}|^2. \quad (7)$$

The self-interaction term stabilizes filled orbitals, and is thus largely responsible for opening up the band gap in transition metal oxides with a partially filled d-shell.

The remaining contribution E_{OR} to the onsite Coulomb interaction is

$$\begin{aligned} E_{OR} = & \frac{1}{2} J_{xc} \sum_R \sum_{\sigma,\sigma'} (-1)^{\sigma-\sigma'} \sum_{k \in \{x,z\}} \\ & \times \left[\left(\sum_{\alpha,\beta} \rho_{\sigma,\alpha,\sigma',\beta,R} \sigma_{\beta\alpha}^{(k)} \right) \left(\sum_{\alpha,\beta} \rho_{-\sigma,\alpha,-\sigma',\beta,R} \sigma_{\beta\alpha}^{(k)} \right) \right. \\ & \left. + \left(\sum_{\alpha} \rho_{\sigma,\alpha,\sigma',\alpha,R} \right) \left(\sum_{\alpha} \rho_{-\sigma,\alpha,-\sigma',\alpha,R} \right) \right]. \quad (8) \end{aligned}$$

The notation $-\sigma$ implies $-\sigma = \uparrow$ for $\sigma = \downarrow$ and vice versa. Similarly $(-1)^{\sigma-\sigma'} = 1$ for $\sigma = \sigma'$ and $(-1)^{\sigma-\sigma'} = -1$ for $\sigma \neq \sigma'$. The term E_{OR} vanishes for a fully spin-polarized system.

The phonons are described by classical amplitudes $Q_{2,R}$ and $Q_{3,R}$ of the two Jahn-Teller active phonon modes.⁴⁴ The Q_2 mode specifies the compression and expansion in the plane perpendicular to the chain (xy -plane). The Q_3 mode describes expansion in z -direction (along the chain), and compression perpendicular to the chain axis,

$$\begin{aligned} Q_{2,R} &= \frac{1}{\sqrt{2}}(d_{x,R} - d_{y,R}) \\ Q_{3,R} &= \frac{1}{\sqrt{6}}(-d_{x,R} - d_{y,R} + 2d_{z,R}). \quad (9) \end{aligned}$$

In contrast to the 3-dimensional model, we suppressed the breathing distortion.

The electron-phonon coupling E_{e-ph} is

$$\begin{aligned} E_{e-ph} = & g_{JT} \sum_n f_n \sum_{R,\sigma} \sum_{\alpha,\beta} \psi_{\sigma,\alpha,R,n}^* M_{\alpha,\beta}^Q(Q_{2,R}, Q_{3,R}) \psi_{\sigma,\beta,R,n} \end{aligned} \quad (10)$$

where g_{JT} is the electron-phonon coupling constant and

$$\mathbf{M}^Q(Q_2, Q_3) = \begin{pmatrix} Q_3 & Q_2 \\ Q_2 & -Q_3 \end{pmatrix}. \quad (11)$$

The phonon energy E_{ph} is given by the term restoring the symmetric octahedron

$$E_{ph} = \frac{1}{2} k_{JT} \sum_R (Q_{2,R}^2 + Q_{3,R}^2), \quad (12)$$

where k_{JT} is the corresponding force constant.

We describe the three majority spin t_{2g} electrons by their classical spin \vec{S}_R . While the direction of the spin may vary, the magnitude of the spin vector equals $|\vec{S}_R| = \frac{3}{2}\hbar$. The spin energy

$$E_S = \sum_R J_{AF} \left(\frac{3\hbar}{2} \right)^{-2} \vec{S}_R \cdot \vec{S}_{R+1} \quad (13)$$

is due to a small anti-ferromagnetic coupling of the spins on neighboring sites.

The spins \vec{S}_R of the t_{2g} electrons are strongly coupled to the spins of the e_g electrons by the Hund's coupling J_H which is described by

$$E_{e-S} = -J_H \sum_n f_n \sum_{R,\alpha} \sum_{\sigma,\sigma'} \psi_{\sigma,\alpha,R,n}^* M_{\sigma,\sigma'}^S(\vec{S}_R) \psi_{\sigma',\alpha,R,n}, \quad (14)$$

where

$$\mathbf{M}^S(\vec{S}) = \left(\frac{3\hbar}{2} \right)^{-1} \begin{pmatrix} S_z & S_x - iS_y \\ S_x + iS_y & -S_z \end{pmatrix}. \quad (15)$$

II.1.1. Parameter determination from ab-initio calculations

The parameters of the model are extracted from ab-initio calculations of the three-dimensional manganites. The details of the calculations are given elsewhere.³¹ Here we summarize the main steps and the results.

We use the projector-augmented wave method⁵⁰ in combination with the local hybrid density functional PBE0r.⁵¹ The free parameters of this functional reflecting the screening of the on-site Coulomb interaction are determined by comparison with experimental x-ray photoelectron spectroscopy (XPS) data.³¹

In order to determine the parameters, we carefully select a set of physically relevant quantities, which are expressed by only a small set of parameters.³¹ We consider the following properties:

1. The energy difference between the fully anti-ferromagnetic and the ferromagnetic phase of CaMnO_3 serves to determine the anti-ferromagnetic coupling parameter J_{AF} .
2. The Hund's rule coupling parameter J_H between t_{2g} and e_g electrons is obtained from the energy separation of the minority and majority-spin e_g -orbital energies of CaMnO_3 .
3. The Jahn-Teller coupling g_{JT} , the Coulomb parameters U and J_{xc} , and the restoring force constant k_{JT} are obtained from the energy levels and the size of the Jahn-Teller distortion in PrMnO_3 .

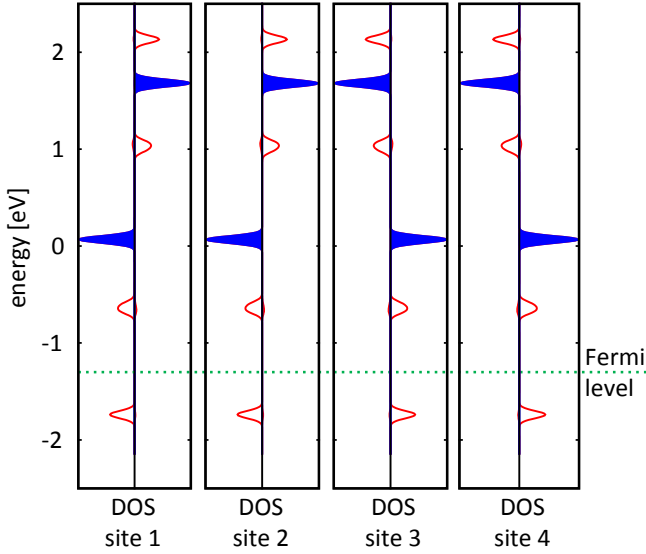


FIG. 2: Density of state for a half-doped one-dimensional manganite for the four sites of the unit cell. The Fermi level is indicated by the horizontal dotted line at -1.3 eV. The true band widths are smaller than the broadening of 0.05 eV. Empty peaks indicate $d_{3z^2-r^2}$ states pointing along the chain, while filled peaks describe the $d_{x^2-y^2}$ orbitals with δ symmetry about the chain axis.

4. The hopping parameters have been extracted from the zeroth and first energy moment of the projected density of states as described elsewhere³¹. The average over the hopping parameters for different magnetic structures of CaMnO_3 , $\text{Pr}_{0.5}\text{Ca}_{0.5}\text{MnO}_3$ and PrMnO_3 , has been taken as parameter t_{hop} .

The values of the parameters are obtained in Ref. 31. For the purpose of this paper we do two changes, namely we ignore the breathing distortion used in the original 3d-model and we increase the antiferromagnetic coupling from 12 meV to 32.6 meV. These changes were necessary to avoid a region in phase space that differs dramatically from the behavior of the 3-dimensional materials. The set of parameters used in this study are given in table I.

J_{AF}	32.6 meV
J_H	0.653 eV
U	2.514 eV
J_{xc}	0.692 eV
g_{JT}	2.113 eV/Å
k_{JT}	5.173 eV/Å ²
t_{hop}	0.585 eV

TAB. I: Model parameters used in the present paper. With two exceptions described in the text, they are identical to the values extracted in Ref. 31 from first-principles calculations of $\text{Pr}_{1-x}\text{Ca}_x\text{MnO}_3$.

II.2. From an effective one-particle description to the many-particle Hamiltonian

II.2.1. Extraction of the one-dimensional model

The model energy expression developed in Eq. (1) describes perovskite manganites in the class $\text{Pr}_{1-x}\text{Ca}_x\text{MnO}_3$. While layered systems exist, we are not aware of manganite materials in which a one-dimensional chain of manganites is embedded into a matrix of a simple large-band-gap oxide. However, in order to develop our approach, i.e., combining the different methods needed for the study of the large range of time scales, we discuss a one-dimensional model manganite based on our findings for the three-dimensional model. This provides a minimal model and is an excellent basis to exercise the methodology and will help us to gain basic insights into the physics of the photodynamics in such systems. While relating to the same parameters as in the three-dimensional calculations, we here limit the model to an infinite, one-dimensional chain of Mn-octahedra. As described below, the first step is to determine the polaronic order and the spin structure for our one-dimensional manganite. The manganite sites form pairs, each of which holds a single electron, which is delocalized over both sites. This structure we refer to in the following as “molecule” or “dimer”. Thus the two sites are spin-aligned. This, together with the resulting displacement pattern of the oxygen atoms, is what is called a Zener polaron. For the half-doped case ($x = 0.5$), a characteristic structure emerges which can be described as a crystal of Zener polarons. Among each other, the Zener polarons are anti-ferromagnetically coupled.

This is the structure encountered by a photon when it is absorbed. Because the time scales of the atomic motion and the spin dynamics are longer than those for the electron dynamics, we freeze atomic and spin structure for the investigation of the photon-absorption process and the subsequent short-time electron dynamics.

In Sec. III.1 we will discuss that in the half-doped case the ground state is dimerized showing a $\uparrow\uparrow\downarrow\downarrow$ magnetic microstructure. Based on this and the short time scale we are considering, the model emerging for the electron dynamics is obtained by freezing $(Q_{2,R}, Q_{3,R}) = (0.2, 0)\text{Å}$ and $\vec{S}_R = \frac{3}{2}\hbar\vec{e}_z\zeta_R$, where \vec{e}_z is a unit vector pointing along the z-axis (without loss of generality, we choose the spins to be aligned along the z-direction), and where ζ_R assumes the values $\dots, +1, +1, -1, -1, +1, +1, -1, -1, \dots$ with increasing R . Hence, the Hund’s coupling responsible for $E_{e,S}$ acts on the electrons like an alternating magnetic field producing a potential. Furthermore, the energies E_{ph} and E_S do not affect the electron dynamics and are omitted.

Thus, the potential energy for our 1D manganite model takes the form

$$\begin{aligned}
E_{\text{pot}}^{\text{1D}} &= \sum_n f_n \sum_{\sigma} \sum_{\alpha, R, \beta, R'} \psi_{\sigma, \alpha, R, n}^* \left(t_{e_g} \delta_{\alpha, a} \delta_{\beta, a} \delta_{|R-R'|, 1} + 2g_{JT} Q_{2, R} (1 - \delta_{\alpha, \beta}) \delta_{R, R'} \right. \\
&\quad \left. - J_H \zeta_R \text{sgn}(\sigma) \delta_{\alpha, \beta} \delta_{R, R'} \right) \psi_{\sigma', \alpha', R', n} + E_U \\
&= E_{\text{kin}} + E_U + \sum_n f_n \sum_R \begin{pmatrix} \psi_{\uparrow, a, R, n}^* \\ \psi_{\downarrow, a, R, n}^* \\ \psi_{\uparrow, b, R, n}^* \\ \psi_{\downarrow, b, R, n}^* \end{pmatrix} \begin{pmatrix} -J_H \zeta_R & 0 & 2g_{JT} Q_{2, R} & 0 \\ 0 & +J_H \zeta_R & 0 & 2g_{JT} Q_{2, R} \\ 2g_{JT} Q_{2, R} & 0 & -J_H \zeta_R & 0 \\ 0 & 2g_{JT} Q_{2, R} & 0 & +J_H \zeta_R \end{pmatrix} \begin{pmatrix} \psi_{\uparrow, a, R, n} \\ \psi_{\downarrow, a, R, n} \\ \psi_{\uparrow, b, R, n} \\ \psi_{\downarrow, b, R, n} \end{pmatrix}. \quad (16)
\end{aligned}$$

This expression is our starting point for deriving an effective Hubbard-like many-particle model.

II.2.2. Basic form of the many-particle Hamiltonian

In second quantization, the terms of Eq. (16) are recast into

$$\begin{aligned}
\hat{H} &= -t_{\text{hop}} \sum_{R, \sigma} \left(\hat{c}_{b, \sigma, R+1}^\dagger \hat{c}_{b, \sigma, R} + \hat{c}_{b, \sigma, R-1}^\dagger \hat{c}_{b, \sigma, R} \right) \\
&\quad + U \sum_{R, \alpha, \beta, \sigma, \sigma'} \hat{c}_{\alpha, \sigma, R}^\dagger \hat{c}_{\beta, \sigma', R}^\dagger \hat{c}_{\beta, \sigma, R} \hat{c}_{\alpha, \sigma, R} \\
&\quad + J_{xc} \sum_{R, \alpha, \beta, \sigma, \sigma'} \hat{c}_{\alpha, \sigma, R}^\dagger \hat{c}_{\beta, \sigma', R}^\dagger \hat{c}_{\alpha, \sigma', R} \hat{c}_{\beta, \sigma, R} \\
&\quad - J_H \sum_{R, \alpha} \left(\frac{3\hbar}{2} \right)^{-1} S_{z, R} \left(\hat{c}_{\alpha, \uparrow, R}^\dagger \hat{c}_{\alpha, \uparrow, R} - \hat{c}_{\alpha, \downarrow, R}^\dagger \hat{c}_{\alpha, \downarrow, R} \right) \\
&\quad + g_{JT} \sum_{R, \sigma} Q_{2, R} \left(\hat{c}_{a, \sigma, R}^\dagger \hat{c}_{b, \sigma, R} - \hat{c}_{b, \sigma, R}^\dagger \hat{c}_{a, \sigma, R} \right). \quad (17)
\end{aligned}$$

In addition, the following points need to be considered. The Jahn-Teller distortion can be considered as static on the femtosecond time scale relevant for an optical transition, so that

$$Q_{2, R} = \frac{g_{JT}}{k_{JT}} \left\langle \sum_{\sigma} \hat{c}_{a, \sigma, R}^\dagger \hat{c}_{b, \sigma, R} - \hat{c}_{b, \sigma, R}^\dagger \hat{c}_{a, \sigma, R} \right\rangle. \quad (18)$$

Under the assumption of perfect orbital polarization, we can evaluate this expression from the occupation, which yields

$$Q_{2, R} \approx \frac{g_{JT}}{2k_{JT}}. \quad (19)$$

Similarly, as mentioned above and based on the findings in Sec. III.1 we freeze the classical spins to the pattern of antiferromagnetic dimers, i.e.

$$\left(\frac{3\hbar}{2} \right)^{-1} S_{z, R} = \dots, 1, 1, -1, -1, 1, 1, -1, -1, \dots \quad (20)$$

with spins aligned along the z-axis.

This gives us the basic form for the many-body model of our 1D manganite.

II.2.3. Effective 1D many-body model for valence electrons in PCMO

Based on the above said, we can now write down the many-body model in a compact form. Due to the classical spin pattern of Eq. (20), we will have a unit cell with four lattice sites, leading us to four bands for the kinetic energy. The hopping is between nearest neighbors only, and the two spin directions interact via a Hubbard-type term. This leads to the effective model sketched in Fig. 3. The Hamiltonian is

$$\hat{H} = \hat{H}_0 + \hat{H}_{\text{int}} \quad (21)$$

with the quadratic single particle terms

$$\begin{aligned}
\hat{H}_0 &= -t_{\text{hop}} \sum_{\sigma \in \mathbb{S}} \sum_R \hat{c}_{\sigma R}^\dagger \hat{c}_{\sigma, R+1} + h.c. \\
&\quad + \sum_{R \text{ odd}} [E_1 \hat{n}_{\uparrow R} + E_2 \hat{n}_{\downarrow R}] + \sum_{R \text{ even}} [E_2 \hat{n}_{\uparrow R} + E_1 \hat{n}_{\downarrow R}]. \quad (22)
\end{aligned}$$

As usual, we introduced the number operator $\hat{n}_{\sigma R} := \hat{c}_{\sigma R}^\dagger \hat{c}_{\sigma R}$, and $\sigma \in \mathbb{S} := \{\uparrow, \downarrow\}$,

The interaction term is the same as in the Hubbard model (HM),

$$\hat{H}_{\text{int}} = U^{HM} \sum_R \hat{n}_{\uparrow R} \hat{n}_{\downarrow R}. \quad (23)$$

Each site in this effective many-body model has two e_g states. The first and fourth site of the unit cell have a spin \uparrow state at the energy E_1 and a spin \downarrow state at the energy $E_2 = E_1 + \Delta$. For the second and third site the spins are reversed. This is captured by rewriting the Hundscoupling as a Zeeman-term in which a magnetic field is aligned along the z -direction and which alternates according to the structure of Eq. (20). This magnetic field leads to a level splitting

$$\Delta = E_2 - E_1. \quad (24)$$

From the difference of the densities $\hat{n}_{\sigma R}$ of up- and down-spin on site R we can, as usual, define the net spin on site R

$$\hat{s}_R^z := \frac{1}{2} (\hat{n}_{\uparrow R} - \hat{n}_{\downarrow R}). \quad (25)$$

Furthermore, the direction of the field due to the staggered spin-dimers on site R is set by Eq. (20), i.e., $\zeta_R := \dots, +1, -1, -1, +1, \dots$.

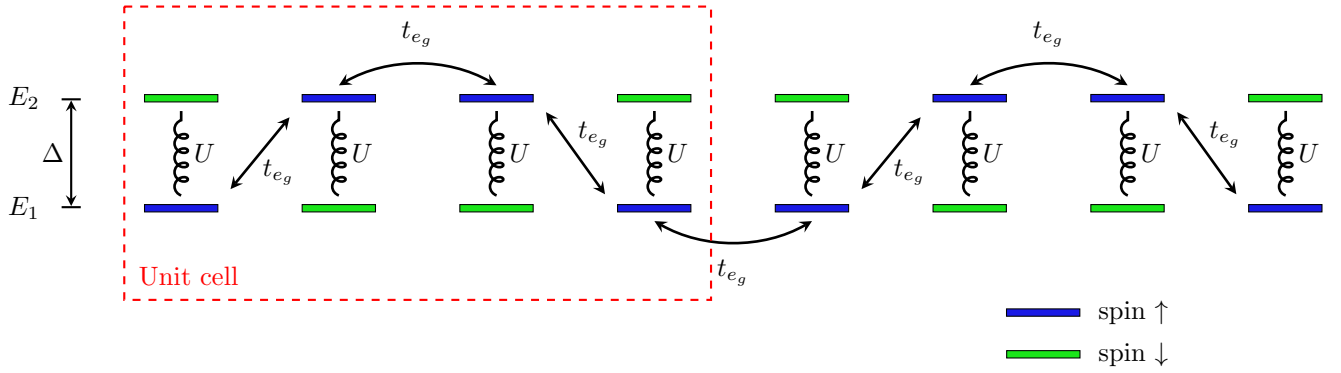


FIG. 3: Sketch of the effective Hubbard-type many-body model derived in this section. The unit cell consists of four sites with each site hosting a spin-up and a spin-down state. The two states are energetically separated by the level splitting $\Delta = E_2 - E_1$. Electrons can hop from one site to another with the hopping amplitude t_{hop} , provided the two states have the same spin. If two electrons are located on the same site they feel the screened Coulomb repulsion U^{HM} . Otherwise this repulsion is screened by the positively charged atoms.

In terms of the ab-initio parameters from Tab. I, the level splitting for our 1D manganite is obtained from the Hunds-coupling and is of the order of $\Delta = 2J_H/t_{hop} \approx 2 \cdot 0.65/0.59 \approx 2.3$. The electrons with spin \uparrow can hop along the spin \uparrow states with hopping amplitude t_{hop} . The spin \downarrow hop along the spin \downarrow state with the same amplitude. If two electrons are on the same site they repel each other because of a screened Coulomb interaction U^{HM} which in terms of the ab-initio parameters is $U^{HM} = (U - 3J_{xc})/t_{hop} \approx (2.51 - 3 \cdot 0.69)/0.59 \approx 0.75$.³¹ Note that in the following we will measure all energies in units of $t_{hop} \equiv 1$.

Note that for the ground state at quarter-filling (i.e., half-doping as in PCMO), the U^{HM} - and Δ -terms do not form competing interactions: for all positive values of the parameters, the charge and spin gaps of the system are finite and the same phase is realized for all values of the parameters as long as U^{HM} is positive. This is easily understood since both terms suppress double occupancy. Therefore, we will focus our investigations using a fixed value of U^{HM} and consider the possibility to obtain different behavior when tuning the value of Δ .

The first effect when varying the value of the staggered magnetic field can be seen in the band structure which we obtain by computing all four single-particle bands from \hat{H}_0 ,

$$\omega_\nu(k) = \pm \frac{1}{2} \sqrt{8 + \Delta^2 \pm 4\sqrt{2(1 + \cos(2\pi k)) + \Delta^2}}. \quad (26)$$

(For the details of the derivation see App. A.) We plot this band structure for various values of the level splitting Δ in Fig. 4. As can be seen, for values $\Delta \gtrsim 4$, the bands are quite flat and the gaps between them substantial, so that we expect for all large values of Δ similar results for the photo excitations. For the pure Hubbard case $\Delta = 0$, we will not have any gaps, but a significant dispersion, so in the regime of small Δ we will have very different behavior. In between, as seen in Fig. 4, we will have

a coexistence of gaps, flat bands, and bands with large dispersion, so that the behavior there will be non-trivial and probably most interesting. Note that the microscopic parameters of Tab. I hint that PCMO would lie in this regime.

Setting $E_1 + E_2 = 0$ w.l.o.g. we can further simplify the quadratic part as

$$\hat{H}_0 = -t_{hop} \sum_{\sigma,R} \hat{c}_{\sigma R}^\dagger \hat{c}_{\sigma,R+1} + h.c. + \Delta \sum_R \zeta_R \hat{s}_R^z. \quad (27)$$

Finally, we also introduce the chemical potential which determines the filling, leading to the final form

$$\hat{H}^{1D \text{ PCMO}} = \hat{H} + \mu \sum_R \hat{N}_R, \quad (28)$$

with \hat{N}_R the total density on site R .

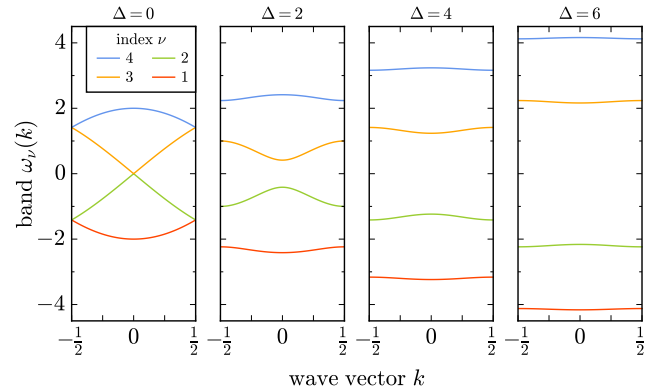


FIG. 4: One-particle band structure of PCMO for different values of the level splitting Δ , which is measured in units of t_{hop} .

II.3. Semiclassical modeling of the light-electron coupling including back action effects

A full quantum mechanical description of the coupling between the light-field and the electrons would require a quantization of the incoming light. This is possible, but will make the treatment more complicated. Often, a simplified approach by directly coupling the time-dependent electric field to the local density or dipole moment³², based on the Peierls-substitution^{21–25} (see Sec. II.4.2) or in terms of the creation of holon-doublon-pairs^{7,26–29} (see Sec. II.4.1) is used. While interesting results have been obtained with these approaches, a major aspect is that the possible back-action of the excited electrons to the light-field is neglected. This, however, can lead to the formation of additional coherences or entanglement between the electrons in the course of the excitation process, and it would be interesting to develop simple approaches capable of taking this into account. Here, we present a simple mean-field or classical approach which is able to take into account the back action to the light-field, but due to its single-particle character can only be considered a starting point for the dynamics of the quantum many-body system, as further described below.

II.3.1. Semi-classical Lagrangian for the coupling of a Klein-Gordon-field to the electrons

We will now introduce a Lagrangian for a semiclassical model which models the light field as well as the interacting electron system of our many-body model (27) on a Hartree-Fock level. The underlying idea is that a photonic wave packet hits the surface and travels down one chain of dimerized PCMO-octahedra. The light enters on the left, excites one site after the other, and finally leaves on the right end of the chain. The electric potential of the light field is described by a one-dimensional real Klein-Gordon field $\phi(x, t)$ with dispersion relation $\hbar\omega(k_\perp) = \hbar c \sqrt{k_\parallel^2 + k_\perp^2}$, where c is the speed of light. This is possible since we are working in 1D and hence the polarization of the light can be neglected. k_\parallel is the component parallel to the surface, and k_\perp perpendicular to the surface. Across a surface k_\parallel is conserved and thus $\hbar k_\parallel$ can be considered as the momentum of a particle of mass M , such that the dispersion relation for the light field reads

$$\hbar\omega(k_\perp) = c\sqrt{(Mc)^2 + \hbar^2 k_\perp^2}. \quad (29)$$

For numerical purposes we consider the Klein-Gordon field as a Fourier-series

$$\phi(x, t) = \sum_k \left[\phi_k(t) e^{i(kx - \omega_k t)} + \phi_k^*(t) e^{-i(kx - \omega_k t)} \right]. \quad (30)$$

The field has a spatial extension in x -direction of L , so that the k -modes are given by $k_l = 2\pi l/L$ with $l \in \mathbb{Z}$.

Each of the N_{mol} dimers in the 1D chain consists of two sites, with one orbital per site. The wave function for orbital $\alpha \in \{1, 2\}$ at dimer $j \in \{1, \dots, N_{\text{mol}}\}$ for spin type $\sigma \in \{\uparrow, \downarrow\}$ is denoted by $|\chi_{\alpha, \sigma, j}\rangle$, the one-particle wave function for electron n is given by $|\varphi_n\rangle$ and is defined as

$$|\varphi_n\rangle = \sum_{\alpha, \sigma, j} |\chi_{\alpha, \sigma, j}\rangle A_{\alpha, \sigma, j, n} \quad (31)$$

$$A_{\alpha, \sigma, j, n} = \langle \chi_{\alpha, \sigma, j} | \varphi_n \rangle. \quad (32)$$

The dimers sit at positions $X_j = j \cdot a$ with lattice constant a .

In addition to the amplitudes $\phi_k(t)$ of the Klein-Gordon field, the amplitudes $A_{\alpha, \sigma, j, n}$ are the main quantities which we use for our modelling and from which equations of motion are derived.

In our modelling, we take into account eight different contributions, each leading to a term in the Lagrangian: (i) the first term describes the Lagrangian density of the Klein-Gordon field ϕ . (ii) coupling of ϕ to the dimers by the dipole-like second term. Note that this is essentially a Stark-term: the spatial derivative of ϕ is an electric field which couples to the polarization of the dimer (i.e., the difference of populations on each of the two atoms, which is given in the single-particle picture advocated here by the differences of the local populations $A_{\alpha, \sigma, j, n}^* A_{\alpha, \sigma, j, n}$). (iii) The time derivatives of the amplitudes $A_{\alpha, \sigma, j, n}$, stemming from the time-dependent Schrödinger equation for the single-particle wave functions (31). The next three terms specify the atomic energies and the hopping: it is assumed that the binding and anti-binding orbitals of each dimer are separated by an energy $2t_{\text{hop}}$ and that the amplitude for both, inter- and intra-dimer hopping, is given by t_{hop} . The atomic energies are included in order to set the energy of the binding orbital to zero. This leads to the terms for (iv) the on-site atomic energies, (v) the intra-dimer hopping, and (vi) the inter-dimer hopping. The next term (vii) models the staggered magnetic field coming from the t_{2g} orbitals, see Eq. (20). Finally term (viii) introduces a Hubbard-like on-site Coulomb interaction with strength U^{HM} which in this one-particle approach is treated in Hartree-Fock (HF) approximation. Writing down the various terms, we hence obtain the Lagrangian

$$\begin{aligned}
\mathcal{L} = & \underbrace{\int_0^L dx \frac{1}{2\kappa} \left\{ (\hbar\dot{\phi})^2 - (\hbar c \partial_x \phi)^2 - (Mc^2 \phi)^2 \right\}}_{\text{(i) Klein-Gordon field for the light-wave in 1D}} + \sum_{n=1}^{N_e} \sum_{j=1}^{N_{\text{mol}}} \sum_{\sigma \in \{\uparrow, \downarrow\}} \left[\underbrace{\lambda \left(\frac{\partial \phi}{\partial x} \right)_{x=X_j} (A_{2,\sigma,j,n}^* A_{2,\sigma,j,n} - A_{1,\sigma,j,n}^* A_{1,\sigma,j,n})}_{\text{(ii) dipole-type coupling between electrons and Klein-Gordon field}} \right. \\
& + \underbrace{\sum_{\alpha=1}^2 i \hbar A_{\alpha,\sigma,j,n}^* \dot{A}_{\alpha,\sigma,j,n}}_{\text{(iii) time derivative of amplitudes from Schrödinger equation}} - \underbrace{t_{\text{hop}} \sum_{\alpha=1}^2 A_{\alpha,\sigma,j,n}^* A_{\alpha,\sigma,j,n}}_{\text{(iv) on-site atomic energies}} + \underbrace{t_{\text{hop}} (A_{1,\sigma,j,n}^* A_{2,\sigma,j,n} + A_{2,\sigma,j,n}^* A_{1,\sigma,j,n})}_{\text{(v) intra-dimer hopping}} \\
& + \underbrace{t_{\text{hop}} (A_{2,\sigma,j,n}^* A_{1,\sigma,j+1,n} + A_{1,\sigma,j+1,n}^* A_{2,\sigma,j,n})}_{\text{(vi) inter-dimer hopping}} - \underbrace{\frac{1}{2} (1 + \sigma \cdot (-1)^j) \cdot \Delta \sum_{\alpha=1}^2 A_{\alpha,\sigma,j,n}^* A_{\alpha,\sigma,j,n}}_{\text{(vii) staggered magnetic field from } t_{2g} \text{ orbitals}} \left. \right] \\
& - \underbrace{\sum_{n=1}^{N_{\text{mol}}} \sum_{\alpha=1}^2 U^{HM} \left(\sum_{n=1}^{N_e} A_{\alpha,\uparrow,j,n}^* A_{\alpha,\uparrow,j,n} \right) \left(\sum_{m=1}^{N_e} A_{\alpha,\downarrow,j,m}^* A_{\alpha,\downarrow,j,m} \right)}_{\text{(viii) on-site Hubbard interaction in Hartree-Fock approximation}}. \tag{33}
\end{aligned}$$

The important part of this ansatz is the coupling of the light field which allows the electrons to absorb energy from *and* emit it back to the Klein-Gordon-field. By considering the Hubbard-interaction in Hartree-Fock approximation, we are hence able of modeling the light-matter interaction in a many-body system including back-action effects without the need of fully quantizing the light-field. The price we have to pay is the restriction to 1D (otherwise the modeling of the electric field of the light via a Klein-Gordon-field would not work), and the mean-field approximation of the Hubbard-interaction. This is a justified approximation, since for a quadratic Hamiltonian in terms of creation and annihilation operators (for example for the Hubbard Hamiltonian in Hartree-Fock approximation) the dynamics generated by the Euler-Lagrange equations obtained from the Lagrangian (33) is equivalent to the dynamics generated by solving the Schrödinger equation of the full system.

In order to obtain an appropriate initial state for the many-body dynamics, we hence need to obtain the time evolution driven by the Lagrangian (33) by solving the coupled Euler-Lagrange equations

$$\frac{d}{dt} \frac{\delta \mathcal{L}}{\delta \phi_k^*} = \frac{\delta \mathcal{L}}{\delta \phi_k^*}, \tag{34}$$

$$\frac{d}{dt} \frac{\delta \mathcal{L}}{\delta \dot{A}_{\alpha,\sigma,j,n}^*} = \frac{\delta \mathcal{L}}{\delta A_{\alpha,\sigma,j,n}^*}. \tag{35}$$

This semiclassical time evolution will provide us the initial state for the tDMRG. This is done in two ways: i) for systems small enough, we extract the many-body state $|\Psi\rangle$ of the system from the single-particle wave functions $|\varphi_n\rangle$ and convert this state into a matrix product state. The conversion from the single-particle state to the many particle state is done by calculating Slater determinants of the $A_{\alpha,\sigma,j,n}$ coefficients. The MPS is obtained from the many body state by the procedure described in Ref. 52. This is done at time t_{MPS} at which the wave packet has travelled through the whole system. ii) For larger systems, we obtain a similar density distribution to the one

resulting from the semiclassical approach at t_{MPS} by applying local operators like Eq. (37) (see below) to the ground state of the system on every molecule within our MPS formalism. This is a further approximation, but will capture the essential features, at least when considering local densities. Note that the time t_{MPS} does not necessarily coincide with the time t_{max} at which the system has absorbed the maximum amount of energy from the field, see Fig. 7 in Sec. III.2.1.

The equations of motion for the Lagrangian in Eq. (33) are derived and integrated in time using a fourth order Runge-Kutta method. For the data presented here, the following parameters are used: The chain is built from four molecules (with two sites per molecule) and four electrons (i.e. quarter filling). For the Klein-Gordon field, 400 k -modes are used to describe the initial wave packet.

II.4. Approaches to photoexcitations without back-action to the light-field

While in the previous section we focused on the possibility to take into account the back-action of the electrons to the light field by introducing a semi-classical approach, here we describe further possibilities frequently considered in the literature to take into account the light-electron interaction without need of quantizing the light-field.

II.4.1. Doublon-holon excitations

Conceptually, the simplest approach to modeling photo excitation is to apply local operators acting directly on the electron distribution.

The first approach we mention by Hofmann and Potthoff²⁷ uses a doublon creation operator

$$\hat{c}_{\uparrow,R}^\dagger \hat{c}_{\downarrow,R}^\dagger$$

on an empty system $|0\rangle$ to create a doublon on site R . This allows to study the decay of the doublon and its spreading with a “light cone effect”.

More interesting in our context would be the creation of particle-hole-like excitations in a system in its ground state and at finite filling. To achieve this, a doublon creation operator

$$d_i^\dagger = \frac{1}{\sqrt{2}} \sum_{\sigma} \hat{c}_{\sigma,i}^\dagger \hat{n}_{\bar{\sigma},i}$$

and similarly a holon creation operator

$$h_i^\dagger = \frac{1}{\sqrt{2}} \sum_{\sigma} \hat{c}_{\sigma,i} (1 - \hat{n}_{\bar{\sigma},i})$$

are introduced.^{7,8,53,54} The photoexcitation is then modeled by applying both operators on the initial state $|\psi_0\rangle$, i.e., $d_i^\dagger h_j^\dagger |\psi_0\rangle$ with i and j often being nearest-neighbor or closeby sites. This approach represents a photoexcitation at half-filling but not at our quarter-filled case because doublons are very improbable due to the site-dependent interactions. While the previous approach creates a localized excitation, in other work, e.g. Ref. 28, it is suggested to model a delocalized holon-doublon pair by considering

$$\hat{X}_L = \sum_{i=0}^{L-1} \sum_{\sigma} \left(\hat{c}_{i,\sigma}^\dagger \hat{c}_{i+1,\sigma} - \hat{c}_{i+1,\sigma}^\dagger \hat{c}_{i,\sigma} \right). \quad (36)$$

Here, we want to study the conceptually simplest excitation and consider the effect of an incoming photon as moving a particle to the neighboring site. Since the photons will not distinguish between the spin directions, we end up with the operator

$$\hat{Y}_i = \sum_{\sigma} \hat{c}_{i,\sigma}^\dagger \hat{c}_{i+1,\sigma}, \quad (37)$$

which is localized on one molecule (which means i is even). As further discussed in Sec. III.2.1, the effect of the incoming light-wave, as modeled by the semi-classical approach, is to shift particles on every other lattice site. This can be captured by applying operator (37) throughout the system on every molecule. This gives us the possibility to study larger systems and consider both, localized excitations by shifting a single electron, as well as excitations throughout the system.

II.4.2. Peierls substitution

Other possibilities to model the photoexcitation are to treat directly the coupling of a classical electrical field to local densities or dipole moments.³² An alternative is to consider the coupling of the vector potential \mathbf{A} to the electrons in the spirit of the Peierls substitution.^{21–25,55} In this approach, the time dependent vector potential of the incoming light wave is captured by minimal coupling $\hat{\mathbf{p}} \rightarrow \hat{\mathbf{p}} - e\mathbf{A}$. Usually, the incoming light-wave is treated as external time-dependent electromagnetic field

to which the back-action of the electrons is neglected. In this way, Peierls substitution leads to a time dependent complex phase factor of the hopping matrix elements and an additional time dependent magnetic field. It is possible to work in a gauge with zero scalar potential, so that $E(t) = -\partial_t A(t)$,^{56,57} a choice which we also make here for convenience. For a tight-binding chain with nearest-neighbor hoppings we hence apply

$$H^{\text{Peierls}}(t) = -t \sum_{i,\sigma} \left(e^{-i \frac{e}{\hbar} \lambda_{i,i+1}(t)} c_{i,\sigma}^\dagger c_{i+1,\sigma} + h.c. \right) + g_S \mu_B \sum_i B_i(t) s_i^z, \quad (38)$$

where the coefficients $\lambda_{i,i+1}$ depend on the vector potential at the positions \vec{R}_i of the lattice sites. For magnetic fields which are not too strong, one finds $\lambda_{i,i+1}(t) = \int_{\vec{R}_{i+1}}^{\vec{R}_i} \vec{A}(\vec{x}, t) \cdot d\vec{x} = (\vec{R}_i - \vec{R}_{i+1}) \cdot \frac{1}{2} [\vec{A}(\vec{R}_i, t) + \vec{A}(\vec{R}_{i+1}, t)]$.

While this is a conceptionally simple way to include the action of the incoming light in the description of a correlated system, however, it remains open how strong the ignored back action of the electrons to the light field might influence the dynamics. Here, we want to address this point by comparing to the dynamics obtained from the semiclassical ansatz of Sec. II.3.1. Possibilities to take into account the back action within the Peierls substitution ansatz would be to explicitly consider the time-dependent vector potential and scalar field resulting from the momentary distribution of charges and currents and recompute from this the complex phase of the hopping term as well as the local fields at each instant of time. A further possibility to take the back action into account is to go beyond the Peierls substitution and, e.g., using the tDMRG, treat the combined system of electrons and photons fully quantum mechanically. This can be done by either quantizing the light field and doing the microscopic calculation, or by treating the electronic system as coupled to a dissipative bosonic bath. Both is possible, in principle, but challenging: the first approach has been used on a one-particle level^{58,59}, the second one can be done, e.g., using the quantum trajectory approach with tDMRG to dissipative systems.³⁸ Since here we are interested in comparing an ansatz not taking into account the back action with one which is considering it, we leave these possibilities for future investigations and choose to compare the two conceptually simple approaches of Eqs. (38) and (33) to each other.

II.5. Details of the tDMRG calculations

For all MPS time evolutions in this paper we use the single site time-dependent variational principle^{40,41} with a time step of $\Delta t = 0.05$ for single excitations and $\Delta t = 0.01$ for multi excitations. Within this method we need to diagonalize the operator exponential of the

time evolution operator

$$\hat{U}(t) = e^{-i\hat{H}\Delta t}, \quad (39)$$

which is done by using the Lanczos algorithm.

As initial state we investigate several options: The groundstate on which we apply an excitation (see Eq. (37)), a state which we obtain from Eq. (35), or a state which is created by a shifting an electron on every other site, leading to a similar state to the one found in Eq. (35).

These calculations yield the fully time-evolved state from which we calculate the one-particle density matrix $\langle \hat{c}_i^\dagger \hat{c}_j \rangle$ at every time step. From this, we obtain the momentum distribution function which then is further analyzed for their quasiparticle content (see Sec. II.6).

Within the time evolution we have two main sources of error: First the error due to the truncation of the Hilbert space to the dimension χ of the matrices of the MPS. In order to control this error, we compared calculations for several values of χ . In all simulations with single site excitations (i. e., applying operator \hat{Y}_i , see Eq. (37) on a central site of the system), a rather small matrix dimension of $\chi = 50$ for system sizes up to 40 sites was sufficient to obtain an error of $\mathcal{O}(10^{-5})$ for the observables. As the entanglement grows with further excitations, a bigger matrix dimension is necessary when considering a globally excited system. In order to counteract that, we choose a smaller systems size of $L = 24$ for the multi-excitation calculations and keep for convenience $\chi = 50$. Since finite-size effects are not pronounced, the behavior observed in these smaller systems does not qualitatively alter so that for the purposes of this paper the system sizes treated suffice. The second source of error is the error due to the Lanczos approximation of the matrix exponential. This error can be controlled by a precision parameter which is in our case set to $\epsilon_{\text{Lanczos}} = 10^{-9}$ and can be neglected since it is much smaller than the error due to the truncation.

The MPS-code used is implemented using the SciPAL⁶⁰ library, which is a framework based on C++ expression templates and which gives the possibility to use CPUs as well as GPUs by calling efficient implementations of BLAS and cuBLAS⁶¹ functions.

II.6. Calculation of the quasiparticle momentum distribution from the tDMRG results

In this section we want to use the numerically exact results for the time evolution obtained by MPS as starting point for a quantum Boltzmann equation (BE). The BE will then provide us with information about the long-time behavior after the excitation, which is inaccessible using numerically exact methods. One important point to realize is that the BE requires as input the quasiparticle distribution function and not the distribution function for the electrons themselves. So as a first step we need to find this quasiparticle momentum distribution from

the tDMRG results, which give the time evolution of the electronic one-particle density matrix (OPDM)

$$\varrho_{\sigma ij}(t) = \text{tr}[\hat{\rho}(t) \hat{c}_{\sigma i}^\dagger \hat{c}_{\sigma j}] . \quad (40)$$

For analyzing the system for possible quasi-particle content we need to compute the time evolution of the momentum distribution function (MDF) which is obtained by Fourier-transforming the OPDM taking into account the 4-band structure of the system. The MDF of each band $\nu \in \mathbb{B}$ is then obtained by using the corresponding transformation of the creation and annihilation operators, see Eqs. (A6) and (A8) in the appendix, leading to

$$n_{\sigma\nu}^{\text{el}}(k, t) = \sum_{\substack{l, l' \in \mathbb{Z} \\ j, j' \in \mathbb{B}}} e^{i2\pi k(l-l')} T_{\sigma\nu j}^*(k) \varrho_{\sigma, 4l+j, 4l'+j'}(t) T_{\sigma\nu j'}(k). \quad (41)$$

In order to obtain an approximate expression for the quasiparticle distribution, we proceed as in Ref. 62 and try to deduce a quasiparticle residue Z , i.e., a jump in the MDF at the Fermi momentum k_F . Even though in 1D at equilibrium Fermi liquid theory breaks down and hence $Z = 0$, we now assume that in an out-of-equilibrium situation the behavior can be described in terms of quasiparticles, as, e.g., demonstrated in Ref. 42. There, for a global quench of a correlated electronic 1D system the quasiparticles are obtained in a flow-equation approach using continuous unitary transformations (CUT) and the resulting time evolution was found to be in excellent agreement with the numerically exact tDMRG results, giving a strong indication for the formation of such quasiparticles due to the quantum quench even in 1D. Here, even though the nonequilibrium situation is different, we assume that quasiparticles in a similar way are created which will show up as a finite quasiparticle residue $Z < 1$ which is formed by the excitation or in the course of the time evolution.

For a Fermi liquid at zero temperature one has the following relation between the distribution function of the electrons $n^{\text{el}}(k)$ and the quasiparticle distribution function $n^{\text{qp}}(k)$ in the vicinity of the Fermi surface:

$$\lim_{k \rightarrow k_F} n^{\text{el}}(k) - \frac{1}{2} - Z \left(n^{\text{qp}}(k) - \frac{1}{2} \right) = 0 . \quad (42)$$

If we use this relation away from the Fermi surface, it defines a k -dependent quasiparticle residue $Z(k)$ that describes the spectral weight of the pole in the one-particle Green's function for momentum k

$$n^{\text{el}}(k) - \frac{1}{2} = Z(k) \left(n^{\text{qp}}(k) - \frac{1}{2} \right) \quad (43)$$

which gives us a means to determine $Z(k)$ from the equilibrium distribution

$$Z(k) = \frac{n^{\text{el}}(k) - \frac{1}{2}}{n^{\text{qp}}(k) - \frac{1}{2}} . \quad (44)$$

We now use (43) as well for the non-equilibrium situation

$$n^{\text{el}}(k, t) - \frac{1}{2} = Z(k) \left(n^{\text{qp}}(k, t) - \frac{1}{2} \right) \quad (45)$$

$$\Rightarrow n^{\text{qp}}(k, t) = \frac{1}{2} + \frac{1}{Z(k)} \left(n^{\text{el}}(k, t) - \frac{1}{2} \right) \quad (46)$$

$$= \frac{1}{2} + \frac{n^{\text{qp}}(k) - \frac{1}{2}}{n^{\text{el}}(k) - \frac{1}{2}} \left(n^{\text{el}}(k, t) - \frac{1}{2} \right) \quad (47)$$

This yields the desired relation between the distribution function of the electrons $n^{\text{el}}(k, t)$ measured by tDMRG and the quasiparticle distribution function of the quasiparticles $n^{\text{qp}}(k, t)$ as input for the Boltzmann equation. The justification for the step from (43) to (47) comes from the continuous unitary transformation approach as used in Ref. 42: $Z(k)$ describes the spectral weight of the electron, which propagates coherently after quasiparticle formation and before the quasiparticle itself decays. The latter timescale is comparable or larger than the inverse scattering rate in the Boltzmann equation, therefore we can use the quasiparticle picture even if it is not strictly applicable in 1d: on the relevant timescale it is a good approximation as verified by comparison with numerically exact results in Ref. 42. Notice that Eq. (47) is only applicable after the short-time regime where quasiparticles form, otherwise it can give unphysical results for $n^{\text{qp}}(k, t)$.

II.7. Linearized multi-band Boltzmann equation for long-time relaxation

Based on the effective model from Sec. II.2.3, Eq. (21), we can investigate the relaxation of the electrons due to electron-electron interactions by means of a quantum BE. We use it in a similar manner as Biebl and Kehrein⁴³, who investigated the thermalization rates of a Hubbard model with next-nearest-neighbor hoppings. Furthermore we perform a linearization of the BE to find the relaxation rates.

To investigate the relaxation of the quasi momentum distribution (QMD) $n_{\sigma\nu}^{\text{qp}}(k, t)$ we use the multi-band quantum Boltzmann-equation (BE)

$$\dot{n}_{\sigma\nu}^{\text{qp}}(k, t) = \mathcal{I}_{\text{coll}}[n^{\text{qp}}]_{\sigma\nu}(k, t). \quad (48)$$

Since we are considering systems without net magnetization, we assume in the following that the spin \uparrow particles have the same QMD $n_{\sigma\nu}^{\text{qp}}(k, t)$ as those with spin \downarrow . Hence, in the following, the spin index σ is not written explicitly any more, i.e. $n_{\nu}^{\text{qp}}(k, t) = n_{\uparrow\nu}^{\text{qp}}(k, t) = n_{\downarrow\nu}^{\text{qp}}(k, t)$.

Thus the collision term is

$$\begin{aligned} \mathcal{I}_{\text{coll}}[n^{\text{qp}}]_1 &= \frac{\pi U^2}{\hbar t_{\text{hop}}} \int_{\mathbb{K}^3} dk_2 dk_3 dk_4 \sum_{\substack{G \in \mathbb{Z}, \\ \nu_{2,3,4} \in \mathbb{B}}} |\Phi_{\vec{\nu}, \vec{k}}|^2 \delta(P_{\vec{k}} + G) \delta(W_{\vec{\nu}, \vec{k}}) \\ &\times \left\{ \underbrace{[1 - n_{\nu_1}^{\text{qp}}(k_1, t)] [1 - n_{\nu_2}^{\text{qp}}(k_2, t)] n_{\nu_3}^{\text{qp}}(k_3, t) n_{\nu_4}^{\text{qp}}(k_4, t)}_{\text{gain term}} \right. \\ &\quad \left. - \underbrace{n_{\nu_1}^{\text{qp}}(k_1, t) n_{\nu_2}^{\text{qp}}(k_2, t) [1 - n_{\nu_3}^{\text{qp}}(k_3, t)] [1 - n_{\nu_4}^{\text{qp}}(k_4, t)]}_{\text{loss term}} \right\}, \end{aligned} \quad (49)$$

where we introduced the set $\mathbb{B} = \{1, 2, 3, 4\}$ containing the band numbers. We defined $\Phi_{\vec{\nu}, \vec{k}}$ as the matrix element of the interaction taken at four momenta in four bands, see Eq. (A14). The momentum is conserved by $\delta(P_{\vec{k}})$ with $P_{\vec{k}} = k_1 + k_2 - k_3 - k_4$, and the reciprocal lattice vector G . Note that the summation over $G \in \mathbb{Z}$ is not an artificial addition, but emergent from the derivation of $\mathcal{I}_{\text{coll}}$. The energy conservation $\delta(W_{\vec{\nu}, \vec{k}}) = \delta(\omega_{\nu_1}(k_1) + \omega_{\nu_2}(k_2) - \omega_{\nu_3}(k_3) - \omega_{\nu_4}(k_4))$ is computed from the one-particle band structure $\omega_{\nu}(k)$, see Eq. (26).

The collision integral of a model describing an infinite lattice naturally allows for Umklapp processes. We account for this by integrating k_4 over a larger region than only the first Brillouin zone. We want to emphasize that this is an exact reformulation of the derived collision integral.

In order to investigate the long time relaxation, we linearize the BE around the thermal distribution $f_{\nu}(k) = 1/\{1 + \exp[\beta(\omega_{\nu}(k) - \mu)]\}$. Hereby β is the dimensionless inverse final temperature and μ the dimensionless chemical potential. In order to perform the linearization we define a perturbation $\phi_{\nu}(k, t)$ by⁶³

$$n_{\nu}^{\text{qp}}(k, t) = \frac{1}{1 + \exp\{\beta[\omega_{\nu}(k) - \mu] - \phi_{\nu}(k, t)\}}. \quad (50)$$

Note that at this point we could also use the numerical results for $n_{\nu}^{\text{qp}}(k, t)$. However, as we will see in Sec. III.4.2, the quasiparticle distribution obtained from the tDMRG is very similar to the electronic one. The conceptually simplest approach is therefore to follow Ref. 43 and assume the quasiparticles to possess a distribution function as in Eq. (50). In future investigations, this can be refined by directly using the numerical results at large enough times.

This leads to the linearized BE

$$\dot{\phi}_{\nu}(k, t) = \hat{\mathcal{L}}[\phi](k, t). \quad (51)$$

The operator $\hat{\mathcal{L}}$ acts on the perturbation ϕ and returns

the change of the perturbation:

$$\begin{aligned} \hat{\mathcal{L}}[\phi]_1 &= \frac{\pi U^2}{\hbar t_{hop}} \int_{\mathbb{K}^3} dk_2 dk_3 dk_4 \sum_{\substack{G \in \mathbb{Z}, \\ \nu_{2,3,4} \in \mathbb{B}}} \delta(P_{\vec{k}}) \delta(P_{\vec{k}} + G) |\Phi_{\vec{\nu}, \vec{k}}|^2 \\ &\times \frac{[1 - f_{\nu_2}(k_2, t)] f_{\nu_3}(k_3, t) f_{\nu_4}(k_4, t)}{f_{\nu_1}(k_1, t)} \\ &\times [\phi_{\nu_1}(k_1, t) + \phi_{\nu_2}(k_2, t) - \phi_{\nu_3}(k_3, t) - \phi_{\nu_4}(k_4, t)]. \end{aligned} \quad (52)$$

$\hat{\mathcal{L}}$ is hermitian in the scalar product

$$\langle \phi, \psi \rangle := \int_{\mathbb{K}} dk \sum_{\nu \in \mathbb{B}} \phi_{\nu}(k) f_{\nu}(k) [1 - f_{\nu}(k)] \psi_{\nu}(k), \quad (53)$$

which induces the norm $\|\phi\| = \sqrt{\langle \phi, \phi \rangle}$. Thence we can represent the perturbation $\phi_{\nu}(k, t)$ by the eigenfunctions $\chi_{\nu}^{(j)}(k)$ and eigenvalues λ_j of $\hat{\mathcal{L}}$:

$$\phi_{\nu}(k, t) = \sum_j A_j(0) e^{-\lambda_j t} \chi_{\nu}^{(j)}(k). \quad (54)$$

The amplitudes $A_j(0) = \langle \phi_{\nu}(k, 0), \chi_{\nu}^{(j)} \rangle / \|\chi_{\nu}^{(j)}\|^2$ are the overlaps of the respective eigenfunction and the initial perturbation $\phi_{\nu}(k, 0)$ at time $t = 0$. The eigenvalues of $\hat{\mathcal{L}}$ are the relaxation rates of the corresponding contribution $A_j(0)$. One can prove that $\hat{\mathcal{L}}$ is positive definite, i.e., its eigenvalues are non-negative. As long as the eigenvalues are positive, the factor $e^{-\lambda_j t}$ leads to the decay of the corresponding contribution of the perturbation $\phi_{\nu}(k, t)$. For $\lambda_j = 0$ the respective part of the perturbation $\phi_{\nu}(k, t)$ does not decay.

There are two eigenvalues, which are zero for any choice of the model parameters: $\chi_{\nu}^{(1)}(k) = \text{const}$, and $\chi_{\nu}^{(2)}(k) = \omega_{\nu}(k)$. For both the factor $[\phi_1 + \phi_2 - \phi_3 - \phi_4]$ in Eq. (52) vanishes. They correspond to conservation of particles and conservation of energy, respectively.

III. GROUNDSTATES, TIMESCALES AND QUASIPARTICLE FORMATION

In this section we are going to explore the behavior of the 1D manganite systems discussed before. In a first step, using ab-initio and MD approaches, we are going to determine the possible GS configurations. We present results in dependence of the doping. From these results, we will focus on the half-doped case as found in PCMO and investigate its behavior following photoexcitation. Four main questions will guide us: i) what is the effect of the photo-excitations of Secs. II.3 and II.4? ii) what characterizes the state and dynamics after the photoexcitation? iii) are quasiparticles formed, and what properties do they have? iv) on which timescales can we expect the system to have relaxed to the final state?

III.1. Polaron and magnetic order in 1-D manganites

The ground state configurations of the one-dimensional manganite chain has been explored using the tight-binding model of Sec. II.1. The ground states have been determined in a two step approach: At first, stable and metastable configurations have been determined using a Car-Parrinello⁶⁴ like dynamics with friction. Secondly, the dominant patterns have been identified. Moving towards a higher-level description the total energy has then be expressed in terms of energies of these patterns.

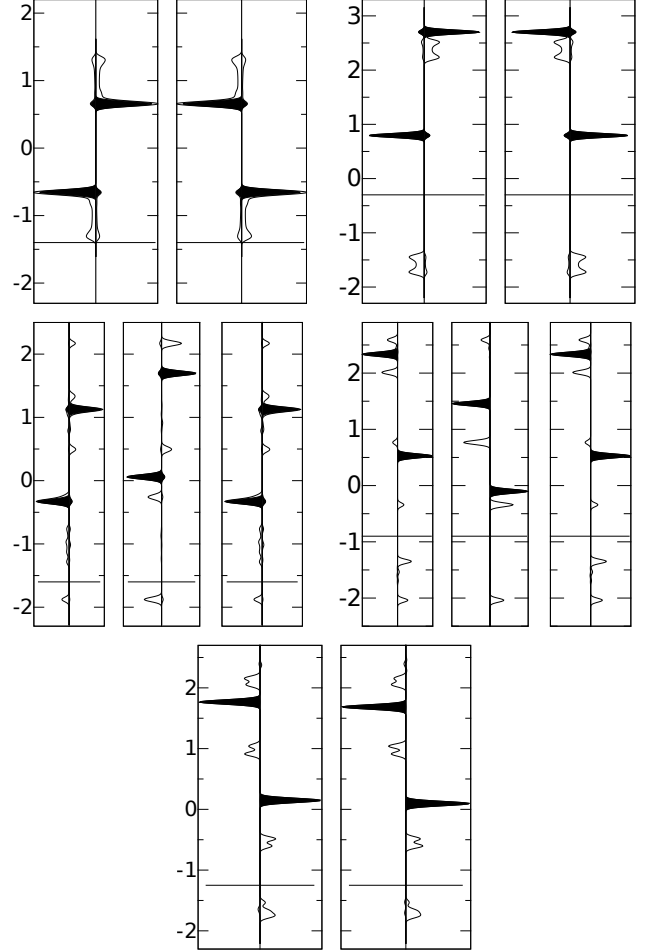


FIG. 5: Projected density of states of the tight-binding model for the polarons in the 1D manganite chain as function of energy in eV. Top-left: Two adjacent unoccupied sites V ; top-right: two adjacent Jahn-Teller polarons P^{JT} , middle left: electron polaron P^e ; middle right: hole polaron P^h ; bottom Zener polaron P^Z . The horizontal line indicates the Fermi level. Empty and filled y lines indicate $d_{3z^2-y^2}$ orbitals pointing along the chain and $d_{x^2-y^2}$ orbitals orthogonal to the chain, respectively. The density of states is broadened.

From our calculations of the tight-binding model for 12-site unit cell of the 1d manganite, we the following

TAB. II: Magnetic orders, polaron composition, deviation $E_{PM} - E_{TB}$ of the energy from the polaron model and energy E_{TB} from the tight-binding model for different number of electrons in a 12-site unit cell of the 1-d manganite. E_{PM} is obtained from Eq. (55).

N_e	magnetic order	composition	$(E - \sum_i E[n_k])[\text{meV}]$	$E[\text{eV}]$
0	$\uparrow\downarrow\uparrow\downarrow\uparrow\downarrow\uparrow\downarrow\uparrow\downarrow\uparrow\downarrow\uparrow\downarrow$	V_{12}	0	-0.3912
1	$\downarrow \uparrow\uparrow\uparrow \downarrow\uparrow\downarrow\uparrow\downarrow\uparrow\downarrow$	$P^e V_9$	0	-1.98129
2	$\downarrow \uparrow\uparrow\uparrow \downarrow \uparrow\uparrow\uparrow \downarrow\uparrow\downarrow\uparrow$	$(P^e V)_2 V_4$	0.5	-3.57088
3	$\downarrow \uparrow\uparrow\uparrow \downarrow \uparrow\uparrow\uparrow \downarrow \uparrow\uparrow\uparrow$	$(P^e V)_3$	10.7	-5.15075
4	$\uparrow\uparrow\uparrow \downarrow\downarrow\downarrow \uparrow\uparrow\uparrow \downarrow\downarrow\downarrow$	P_4^e	59.3	-6.69231
5	*1 non-collinear	$P_3^Z P_2^e$	-16.2	-8.08389
6	$\uparrow\uparrow \downarrow\downarrow \uparrow\uparrow \downarrow\downarrow \uparrow\uparrow \downarrow\downarrow$	P_6^Z	0	-9.38383
7	$\uparrow\uparrow \downarrow\downarrow \uparrow\uparrow \downarrow\downarrow \uparrow\uparrow \downarrow\downarrow$	$P_4^Z P^h P^{JT}$	-46.7	-10.46353
8	*2 $\uparrow \uparrow\uparrow \downarrow\uparrow\downarrow \uparrow\uparrow \downarrow \uparrow\uparrow$	$P_3^Z P^h P_3^{JT}$	-12.0	-11.51915
9	*3 $\uparrow\uparrow \downarrow \uparrow\uparrow \downarrow\uparrow\downarrow \uparrow\uparrow\uparrow \downarrow$	$P_2^Z P^h P_5^{JT}$	-68.9	-12.51556
10	$\uparrow\downarrow \uparrow\downarrow \uparrow\downarrow \uparrow\downarrow \uparrow\downarrow \uparrow\downarrow$	$P_2^Z P_8^{JT}$	-74.4	-13.51869
11	$\downarrow \uparrow\uparrow\uparrow \downarrow\uparrow\downarrow\uparrow\downarrow\uparrow\downarrow$	$P^h P_9^{JT}$	0	-14.47726
12	$\uparrow\downarrow\uparrow\downarrow\uparrow\downarrow\uparrow\downarrow\uparrow\downarrow\uparrow\downarrow$	P_{12}^{JT}	0	-15.47453

*1- All the angles between classical spin vectors lie in the range of $\sim (162 - 175)^\circ$.

*2- The average angle within the trimer is $\sim \langle 51^\circ \rangle$ and other angles are in the range $\sim (157 - 166)^\circ$.

*3 - The average angle within the trimer is $\sim \langle 39.5^\circ \rangle$ and other angles are in the range $\sim (162 - 175)^\circ$.

dominant patterns, which we describe as polarons.

1. There are vacant sites V without electrons. These sites interact only weakly by a Heisenberg-exchange coupling J_{AF} . In this language, the electron-poor manganite analogous to CaMnO_3 would consists of tightly packed vacant sites.
2. The electron polaron P^e , which is a trimer of ferromagnetic Mn sites occupied by a single electron. The electron polaron is analogous to an electron polaron in the electron poor CaMnO_3 -like phase. In the electron polaron, a single electron is spread over three sites. Such a polaron has three electron states in the majority-spin direction: The occupied state is fully bonding. The second state is non-bonding. It is distributed only over the two outer sites of the trimer. The third state of the electron polaron is fully antibonding.
3. The Zener polaron P^Z is a dimer of two ferromagnetically aligned Mn sites, which share a single electron. The half-doped material analogous to $\text{Pr}_{1/2}\text{Ca}_{1/2}\text{MnO}_3$ can be described as a crystal of antiferromagnetically coupled Zener polarons. The Zener polaron has two states in the majority spin direction: a filled bonding and an empty antibonding state.
4. The hole polaron P^h , which is a trimer ferromagnetically aligned Mn sites occupied by two electrons. The hole polaron is analogous to a hole polaron in the electron rich PrMnO_3 -like phase. It has the same three states as the electron polaron,

but now also the second, non-bonding states is occupied.

5. The Jahn-Teller polaron P^{JT} is an electron that occupies a single site. A crystal of Jahn-Teller polarons is analogous to PrMnO_3 .

In order to extract the energies for these structural units, we start out setting the reference μ_0 for the electron chemical potential to the coexistence value of the electron-poor ($N_e = 0$) and the electron rich ($N_e = N_s$) systems that are analogous to CaMnO_3 and PrMnO_3 respectively. With N_s we denote the number of sites in the unit cell and with N_e the number of electrons per unit cell. We obtain $\mu_0 = -1.25694417$ eV. Then we identify the polaron composition from the magnetic order. Magnetic order and resulting composition are given in table II. The formation energies of the defects are determined such that the energy of the polaron model

$$E_{PM}[n_V, n_e, n_Z, n_h, n_{JT}] = \sum_{k \in \{e, Z, h, JT\}} n_k (E_f^{(k)} + \mu_0 N_e^{(k)} - J_{AF}) \quad (55)$$

matches the total energies obtained from the tight-binding calculation given in table II. With n_k we denote the number of polarons $P^{(k)}$ where $k \in e, Z, h, JT$ denotes the polaron type. With $E_f^{(k)}$, we denote the polaron formation energy of and with $N_e^{(k)}$ the number of electrons it contains. The values are given in Tab. III. The polaron formation energies have been extracted so that the energies of the model calculations are reproduced by Eq. (55) for $N_e = 0, 1, 6, 11, 12$. The energies of these structural units are given in Tab. III.

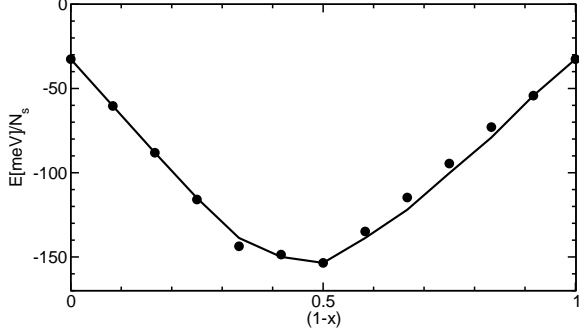


FIG. 6: Energy per Mn-site of the model calculation (line) as function of the electron occupation $1 - x = N_e/N_s$ compared to the sum of polaron energies given in Eq. (55). The energy $(1 - x)\mu_0$ of the particle reservoir has been included.

TAB. III: Formation energies of polarons, number $N_s^{(k)}$ of sites occupied by the polaron P^k and number $N_e^{(k)}$ of electrons on it.

polaron	V	P^e	P^Z	P^h	P^{JT}
$E_f^{(k)}$ [meV]	0	-398.3	-274.4	-324.9	0
$N_s^{(k)}$	1	3	2	3	1
$N_e^{(k)}$	0	1	1	2	1

The mechanism limiting the size of the electron polaron is the competition of the kinetic energy with the antiferromagnetic coupling. The maximum size of the electron polaron is reached, when the delocalization energy gained by extending the electron polaron by one site is exceeded by the antiferromagnetic coupling. In the limit of large Hund's rule coupling J_H , the size of the polaron is thus determined by the ratio t_{hop}/J_{AF} of hopping parameter and antiferromagnetic coupling. With our set of parameters this maximum size is three sites.

The Coulomb interaction makes a direct contact between electron polarons unfavorable, which explains the observation that electron polarons in the dilute limit are separated by at least one vacant site.

Because of the kinetic energy cost, the smaller polarons are energetically less favorable than larger polarons. Thus they become relevant only when the electron density is such that the larger polarons are densely packed. For our system this occurs at $N_e/N_s = 1/3$.

Beyond this value, electron polarons P^e and Zener polarons P^Z coexist until Zener polarons are densely packed. This is the case for half-doping, i.e. $N_e/N_s = 0.5$. This is the doping used for the study of the optical excitation.

In the electron rich phase, the system forms a solid of antiferromagnetically coupled Jahn-Teller polarons.

The favorable defect for doping the electron-rich phase

with holes is the Zener polarons. This is different from electron doping the electron-poor manganite, where the extended defect P^e more favorable than the Zener polaron. The formation of hole polarons P^h requires substantial energy

$$P^{JT} + P^Z \rightarrow P^h + 50.5 \text{ meV} . \quad (56)$$

The hole polaron is, however, formed in response to spin frustration. The insertion of a hole into the electron rich material by forming a Zener polaron would, at the same time, introduce a domain wall into the antiferromagnetic order. An isolated domain wall can either annihilate with another domain wall or combine with a Zener polaron to form a hole polaron. With the hole polaron, we identified a structural unit which does not contribute to the ground state at zero Kelvin, but plays an important role for the interconversion of polarons.

The nature of an isolated domain wall can be rationalized from the point of view of a Zener polaron. An abrupt domain wall in the electron rich material is equivalent to a Zener polaron with one additional electron. The additional electron enters into an antibonding state, which is energetically highly unfavorable. By forming a hole polaron, this electron is transferred into the non-bonding state of the hole polaron, which is energetically favorable.

However, the occurrence of non-collinear spin arrangements indicates that the phase boundary can also delocalize and form a spin spiral.

Combining sites into structural units such as polarons is analogous to the formation of molecules out of atoms. The energy scale of forming the polarons is of the order of 0.3 eV. The conversion of polarons into each other is analogous to chemical reaction and this energy is already smaller than the energy per polaron itself. An example for such a reaction between polarons is the formation of a hole polaron from a Jahn-Teller and a Zener polaron in Eq. (56). The interaction between polarons is then limited to a substantially smaller scale defined by the Heisenberg exchange J_{AF} , respectively the antiferromagnetic coupling of Jahn-Teller polarons. The energy scale for the interaction between polarons is of order 10 meV.

In this section, a coarse grained description is obtained from the tight binding model. Such models are valuable for mapping out the dynamics of the polaronic and magnetic order in large length and time scales.

III.2. Effect of the photoexcitations

Now we turn to the effect of the different approaches to photoexcitations and focus on the half-doped case of PCMO. Since by construction the excitations described in Sec. II.4.1 either create a doublon-holon-pair or simply shift one particle, we are not going to discuss their effect on the ground state here, but rather focus on the results obtained from applying the semiclassical description of Sec. II.3.1 and the results from the Peierls-substitution Sec. II.4.2. Throughout this section we work in units in which the hopping matrix element is set to one, $t_{hop} \equiv 1$.

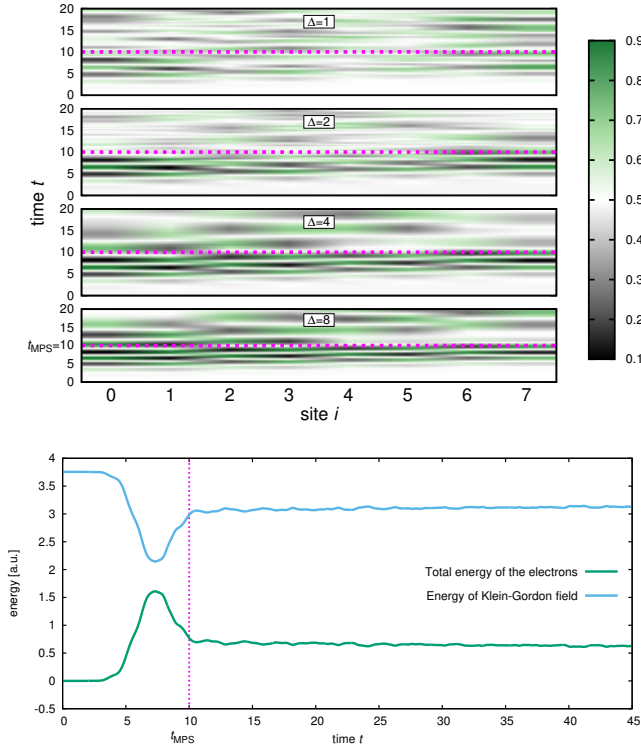


FIG. 7: (a) Time evolution of the particle density during the photoexcitation modeled by the semiclassical Lagrangian Eq. (35) for the different values of Δ as indicated. (b) Energy of the Klein-Gordon field and of the electrons. At time t_{MPS} the original wave packet has left the system and the system is considered as excited.

III.2.1. Semiclassical approach

Figure 7 shows the main result of this section for a system with $L = 8$ sites, on-site interaction $U^{HM} = 3$ and four different values of Δ . Larger systems display a very similar behavior so that it is sufficient to discuss small systems here. As can be seen in Fig. 7(a), the main effect of the incoming light-wave is to induce a density-modulation throughout the system which can lead to maximal polarization (i.e., occupation $\langle n_i \rangle = 0$ and $\langle n_i \rangle = 1$ on neighboring sites) in the course of time, if the amplitude of the external field is chosen high enough. Initially energy is taken from the Klein-Gordon field, but towards the end of the excitation it is also emitted back to it. The emerging picture is the following: As soon as the wave packet encounters a molecule, the electron, which is delocalized over the molecule, starts to oscillate between localized and delocalized states. Each of the molecules acts as a small antenna, and for $\Delta \gg t$ one can imagine a set of decoupled small antennas which get fully polarized by the incoming light. This oscillation of the charges itself now acts as an emitter, and energy is emitted both, back to the electric field, and to the next molecule.⁶⁵ Note that the latter is not captured by the Peierls-substitution

ansatz: the back-action to the light-field can hence lead to a stronger effective field throughout the system and hence a stronger response than in the Peierls-substitution treatment. This will be discussed in more detail further below. At first the energy of the molecules increases due to the interaction with the Klein-Gordon field, see Fig. 7(b) for the case $\Delta = 2$. As the molecules cannot only absorb energy from the field but can also radiate back into the field, the energy of the molecules decreases again and approaches the initial value. The maximum in the absorbed energy is found after three of the four molecules were hit by the wave packet (in Fig. 7(b) at time $t_{\text{max}} \approx 7.5\hbar/J$).

After time $t_{\text{MPS}} \approx 10\hbar/t_{\text{hop}}$ (for $\Delta = 2$) the wave packet has traversed the last molecule in the chain (dotted magenta line in Fig. 7). The many-body state at this time is then used as a starting point for the tDMRG calculations, see section III.3. This, however, can only be done for very small systems. In order to emulate the behavior of the semi-classical light excitation for larger systems, we will study below a simplified situation in which we assume a full polarization of the molecules is achieved by subsequently applying the operator Eq. (37) to each molecule.

III.2.2. Peierls-substitution

In Fig. 8 we display our results obtained with the Peierls substitution Eq. (38) for different values of Δ . The electric field is prepared as a wave packet with maximum amplitude $\mathcal{E}_0 = 20J/(ea)$, where J is the hopping amplitude, a the lattice constant and e the elementary charge. The central wave vector k_0 of the wave packet corresponds to a wavelength of $\lambda_0 = 500\text{nm}$. Because the length scales of the lattice constant a and the wave length λ_0 differ by at least five orders of magnitude, the spatial extension of the wave packet is much larger than the length of the atomic chain. Therefore, at one instance of time, every site feels approximately the same external field. The speed of light is set to a realistic value and the center of the wave packet interacts with the chain at time $t_0 = 4$. Due to the finite width of the wave packet, the interaction lasts approximately until time $t_F = 8$. Remarkably, while at the first glance the results seem quite different from the ones obtained with the semi-classical approach, the underlying behavior is the same: the main effect in both cases is to induce a polarization in such a way that on every second molecule an electron is moved to the left or to the right, respectively. However, while in the semiclassical approach the charge redistribution appeared quite uniformly throughout the system, here the strongest effect is seen at the boundaries, while in the bulk (unless Δ very small), nearly no effect is visible. This seems to be related to the density profile of the finite system shown in Fig. 9: despite the finite value of Δ , oscillations of the density similar to the Friedel-like oscillations of the Luttinger-liquid state of the Hubbard chain at quarter filling⁶⁶ remain, even though decaying much

faster. This unequal distribution of charges seems to act as local antennas at which the incoming light field acts strongest, leading to a more pronounced density redistribution at the edges than in the bulk, where the density oscillations die out. This is also seen in the fact that the effect of the light-field is weakened when increasing Δ : in the gapless Luttinger-liquid case with $\Delta = 0$ the density-oscillations in the ground state are strongest, and the charge redistribution due to the light-field is strongest. For larger values of Δ , however, it is much weaker for the same amplitude of the light field. Note, however, that the Peierls-substitution ansatz directly acts on the hopping amplitudes, without explicitly taking into account the values of the local densities. This is interesting and needs further investigations. Also note for $\Delta = 4$ the resonance at time $t \approx 6$. This is also seen for close values of Δ and seems to be a resonance which needs to be further explored. Since this would go beyond the scope of this paper, we leave it to future investigations.

To better understand the different behavior of the Peierls-substitution and the semiclassical excitation, let us have a closer look at the case $\Delta = 0$ and compare Fig. 8(d) to Fig. 7(a). While in the latter case an artificially slow light-field was assumed to better resolve the local effects, in Fig. 8(d) we considered the light-field to travel through the system with realistic parameters, i.e., the speed of light, so that the excitation appears instantaneous. However, besides this and the stronger effect at the edges, the excitation leads to a similar redistribution of charges, i.e., also in the modeling of the photoexcitation by the Peierls-substitution we get the same local polarization of the system, even though with a smaller amplitude in the bulk. This smaller amplitude can be understood in terms of the missing back action to the light-field: within the Peierls-substitution, the electrons do not emit any electromagnetic waves. Therefore, compared to approaches taking into account the back action, a weaker electric field is acting on the charges, leading to a smaller response, unless the polarization is large as induced by the Friedel-like oscillations mentioned before. In the following, we will therefore continue our considerations based on the findings obtained by the semi-classical approach.

III.3. Short-time dynamics after the photoexcitation

Now we turn to the many-body dynamics of initial states as obtained by photoexcitation. Based on the findings described above, we take on the picture that the photo-excitation in our 1D manganite system essentially shifts electrons by one site. In this spirit, we first discuss the basic behavior of an excitation in which we shift only one single electron to the neighboring site by applying operator Eq. (37) in the center of the system to its ground state. Afterwards we go to the dynamics of more complicated initial states obtained from the semiclassical approach or by shifting an electron on each molecule.

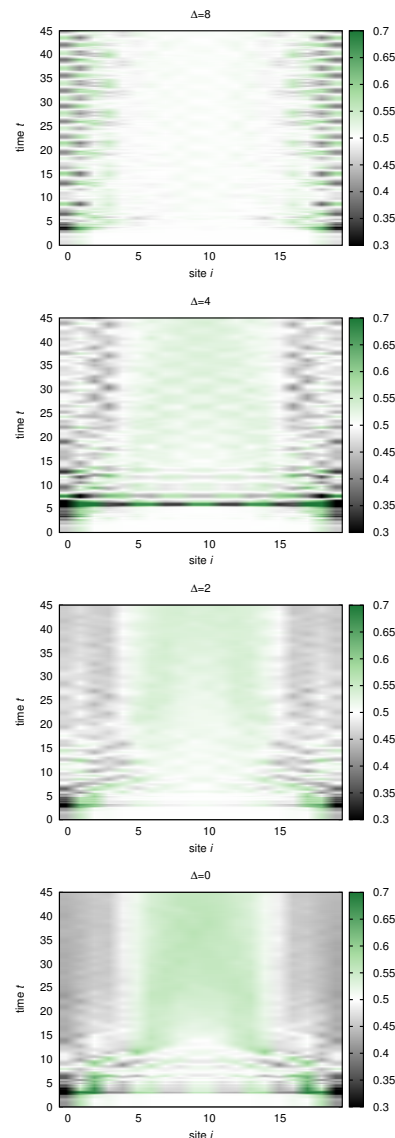


FIG. 8: Results of the photoexcitation modeled by the Peierls substitution ansatz, Eq. (38) for different values of Δ as indicated. The results are obtained by tDMRG for systems with $L = 24$ lattice sites and $U^{HM} = 3$, and the values of the electrical field as indicated in the text.

III.3.1. Dynamics of a single particle excitation

In Fig. 10 we show our DMRG-results for the time evolution of the local density $\langle n_i \rangle$ at the site of the excitation in the center of the system after applying operator Eq. (37) to the ground state of the system. We display results for different values of Δ and keep $U^{HM} = 3$ fixed, assuming that the concrete value of the Coulomb-interaction will not qualitatively change the behavior. As can be seen, three different regimes can be identified: at very large Δ , strong oscillations and a beating-effect are obtained. This can be understood in terms of the magnetic field being so strong that the energy of the electrons does not suffice to tunnel to the next molecule, i.e.,

one deals with weakly coupled dimer systems which act as very small, but deep potential wells. The behavior in this regime is hence dominated by the oscillation of a single electron within the potential wells (we are at quarter filling) and a tunneling out of them with a small rate due to the weak coupling to the next potential well. The interference effects coming from this motion lead to the beating. This type of excitation is long-lived (see Fig. 11) and is reminiscent of the creation of a localized electron-hole pair which keeps its stability in time not due to nearest-neighbor interactions as, e.g., in Ref. 26, but due to the structure of the alternating magnetic field imposed by the t_{2g} electrons of the manganite material. This is an interesting observation and shows that long-lived exciton-like excitations can be stabilized by a convenient configuration of the electrons not participating in the charge transfer, as in our case due to the perovskite-structure and the Jahn-Teller effect (i.e., electron-phonon coupling). This indicates that correlation effects by the formation of magnetic microstructures can have an indirect, but strong influence on the lifetime of the excitations.

The second regime we want to highlight is the opposite case with $\Delta = 0$, i.e., a 'manganite-material' in which the perovskite-structure and the electron-phonon-coupling do not lead to an 'interesting' environment for the electronic transport. Here, we are dealing with the dynamics of such an excitation in a Luttinger liquid at quarter filling. As can be seen, the excitation disappears very quickly (on a time scale $t_{\text{relax}} < 10$ in units of the inverse hopping, corresponding to $t_{\text{relax}} < 12\text{fs}$ using the parameters of table I) and the system relaxes quickly to its initial state (up to small oscillations). This can be understood in terms of ballistic transport of the quasi-particle(s) created which move with a velocity similar to the Fermi-velocity through the system.^{67–69} A further analysis of this scenario is discussed below.

Interestingly, an intermediate regime can be identified, in which the alternating magnetic field is not having such a strong effect that we can think of independent potential wells, but in which the potential wells are coupled strongly enough with each other so that we obtain non-trivial dynamics. This is displayed in Figs. 10 and 11

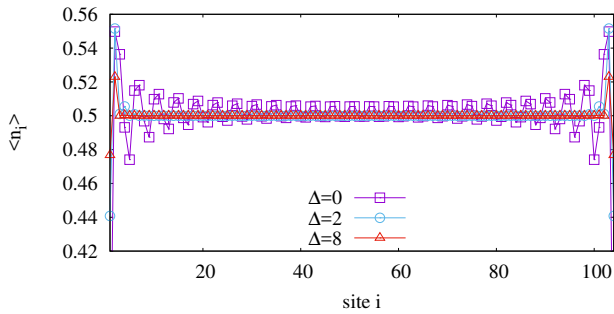


FIG. 9: Local density in the ground state for different values of Δ at $U^{HM} = 3$ for a system with $L = 104$ sites obtained by DMRG.

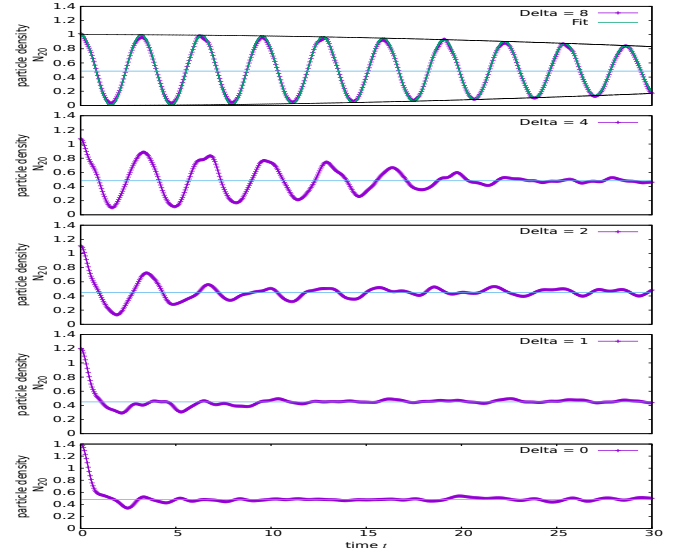


FIG. 10: tDMRG-results for the relaxation of a single excitation at different values of Δ for $U^{HM} = 3, L = 40$. The plots display the time evolution of the local density on the site at which an electron was shifted by applying the operator Eq. (37) to the ground state for the values of Δ as indicated. The lines show fits using $f(x) = \frac{1}{4}(\cos(ax) + \cos(bx)) + \frac{1}{2}$ to estimate the time scale on which the excitation decays.

for $\Delta = 2$. In this case, oscillations of a larger amplitude are seen which are rather long-lived and which are not finite-size effects. According to Tab. I, this is the regime relevant for PCMO, indicating that one may expect a non-trivial dynamics following photoexcitation in this and related materials.

III.3.2. Many-body dynamics following the semiclassical excitation process

The considerations of the previous sections gave us some basic insights into the behavior of the system when the photo-excitation would induce the shift of a single electron. Now we want to turn to the situation where we consider the time evolution fully quantum-mechanically using MPS techniques after we excited the whole system in the way described in Sec. II.3.1. As described there, to use the state after the photoexcitation and then apply MPS methods on it can only be done for very small systems directly. In Fig. 12 we show our results for $\Delta = 2$ and $\Delta = 8$ for the time evolution of the local densities and the local currents. As can be seen, in the case of large Δ , the currents oscillate essentially between two sites, and charge transport between the molecules is widely suppressed. This effect becomes even more pronounced if the value of Δ is increased. The small currents within molecule 3, i.e. the current over the bonds 4 and 5, can be explained by looking at the particle density in Fig. 13: the density on this molecule oscillates only slowly around 0.5 in this time range, before higher oscil-

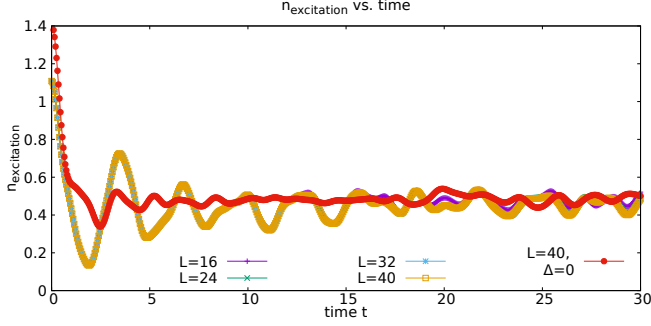


FIG. 11: Time evolution of the local density on the site of the excitation for $\Delta = 2$ and $U^{HM} = 3$ which is close to the parameters of table I. The plot compares MPS results for systems with $L = 16$ (violet crosses), $L = 24$ (green x), $L = 32$ (blue asterisk), $L = 40$ (beige empty squares), and $L = 40$ for $\Delta = 0$ (red filled circles). The results displayed are obtained with MPS matrix dimension $\chi = 50$ and are identical with results obtained with $\chi = 100$ compared to at shorter times. The results for the different system sizes at $\Delta = 2$ are nearly identical up to times $t \approx 15$, and also afterwards show only small finite-size effects for the times displayed. In contrast to the $\Delta = 0$ case, for $\Delta = 2$ the oscillations are more pronounced, indicating a longer life-time of the excitation.

lations – and therefore also higher current – start again around time $t \approx 20$. As discussed above in the case of a single excitation, this ‘trapping’ due to the magnetic microstructures leads to the long time scales on which these exciton-like excitations can be identified. In Fig. 13 we display the long-time behavior of the small system as obtained by MPS after initial excitation by the semiclassical approach. The plot displays results up to time $t_{\max} = 300$ in units of the hopping, which using the parameters of Tab. I corresponds to $t_{\max} \approx 340\text{fs}$. As can be seen, the behavior does not change substantially with time. However, slow oscillations of the particle density on time scales $t = \mathcal{O}(200\hbar/t_{eg})$ ($\Delta = 8$) and $t = \mathcal{O}(25\hbar/t_{eg})$ ($\Delta = 2$) are seen, which represent the beating-effect mentioned before. On these time scales particles leak into neighboring molecules. As no monotonically decaying envelope can be identified, the time scales which can be reached with our numerical approaches are not long enough to estimate the lifetimes of these excitations. This will be pursued in Sec. III.5 using a linearized BE ansatz.

III.3.3. Dynamics of the local density after a multi particle excitation

In Fig. 14 we present our result for the time evolution of the local density at the central site of the system after applying operator Eq. (37) on every other site to the ground state of the system at $U = 3$ and the different values of Δ indicated. By comparing to Fig. 10 we see that – at least for the dynamics at the center of the sys-

tem – the essential behavior seems to be captured rather well by considering a single excitation on only the lattice site of interest. In particular, one again observes that the dynamics shows differences in the three regimes of very large, very small, and intermediate values of Δ . In the following we will, therefore, consider the time evolution of the momentum distribution functions at large and intermediate values of Δ and further explore the differences in the dynamics following a single and a multi-site excitation.

III.4. Momentum distributions for electrons and quasiparticles

In the previous section we identified three typical regimes of the time evolution by considering local quantities, and in particular found that the parameters of Tab. I obtained for our 1D-PCMO model indicate that the material should be in a rather interesting regime. In this section, we are going to further analyze this behavior by asking for the quasiparticle content emerging due to the

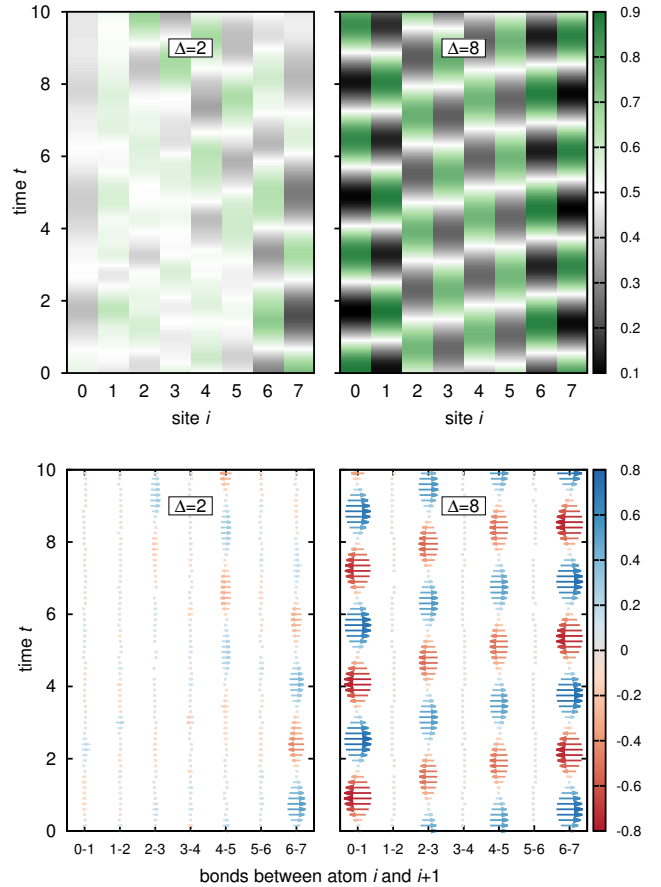


FIG. 12: (a) Time evolution of the particle density starting from an initial state obtained with the semiclassical approach of Sec. II.3.1 obtained by tDMRG for $\Delta = 2$ and $\Delta = 8$. (b) Time evolution of the local currents for the same setups obtained from tDMRG.

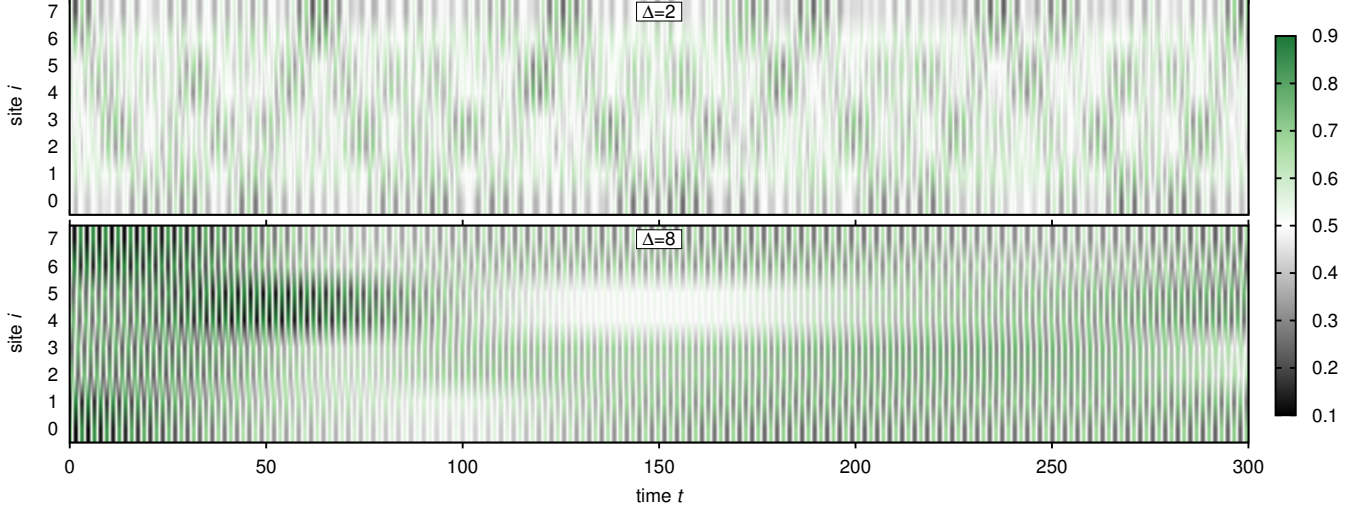


FIG. 13: Time evolution of the particle density using tDMRG starting from an initial state obtained from the semi-classical treatment of the photoexcitation. Top: $\Delta = 2$; bottom: $\Delta = 8$.

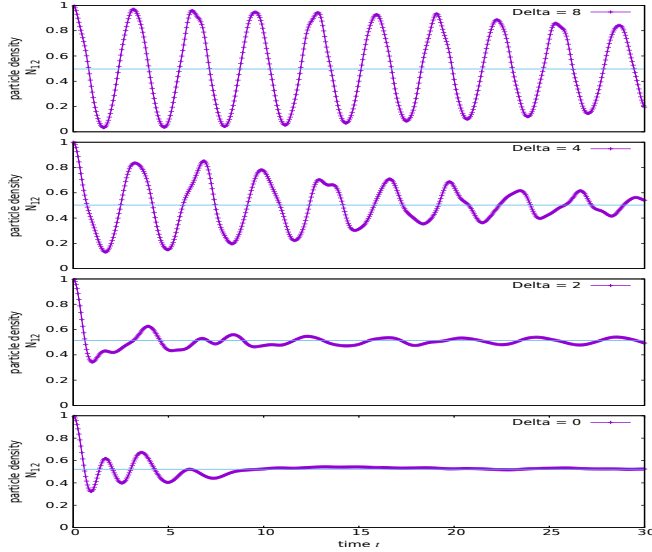


FIG. 14: tDMRG-results for the relaxation of a multi-site excitation obtained by applying operator Eq. (37) on every other site on the ground state of the system at the different values of Δ as indicated for $U^{HM} = 3$, $L = 24$ and keeping a matrix dimension $\chi = 50$. The plots display the time evolution of the local density at the central site.

excitation, and its evolution with time. For this, we will now shift our focus to the momentum distribution function and the quasiparticle-MDF obtained as described in Sec. II.6.

III.4.1. Momentum distribution function of the electrons

In Figs. 15 and 16 we compare the MDF of the system in its ground state with the one directly after exciting it by applying operator Eq. (37) to the central site of the system for $\Delta = 8$ and $\Delta = 2$, respectively. Let us first discuss the MDF of the ground state. Since we are at quarter filling, as expected, the first band $\nu = 1$ is highest populated, and the population of the higher bands is negligibly small. However, note that for computing the MDF, we build on the single-particle band structure of Eq. (26) obtained at $U^{HM} = 0$. Note that the population in the first and fourth band increases with $|k|$, and in the second band is a non-monotonous function of k . This unusual behavior we associate to the finite value

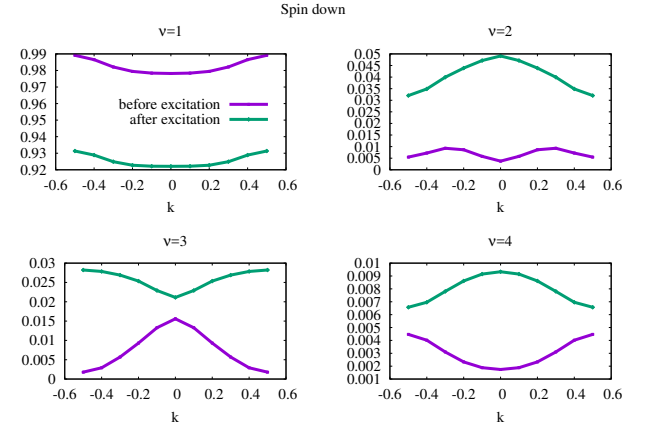


FIG. 15: DMRG results for the momentum distribution function for a system with $L = 40$, $\Delta = 2$ and $U^{HM} = 3$ before (magenta) and just after (green) the photoexcitation by applying operator Eq. (37) at the center of the system.

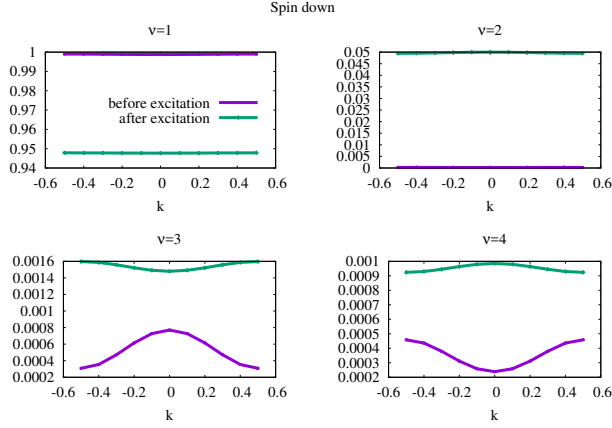


FIG. 16: DMRG results for the momentum distribution function for a system with $L = 40$, $\Delta = 8$ and $U^{HM} = 3$ before (magenta) and just after (green) the photoexcitation by applying operator Eq. (37) at the center of the system.

of U^{HM} : the Hubbard-interaction will lead to a renormalization of the parameters of the bands, in particular also of the value of Δ , which leads to the observed distortions. It would be necessary to perform a many-body calculation of the one-particle spectral function to get the distribution in all details, which goes beyond the scope of the present paper and which is left for future investigations. Here, we pursue a simpler path and consider the time evolution of the single-particle bands and their populations as indicators for the strength of the scattering between the bands in the course of the time evolution, and later also to compare the quasiparticle distributions to the electronic MDF.

The effect of the photoexcitation is to move particles from the lowest band to the higher ones. While for $\Delta = 2$ the second and third band get a higher population, the one of the fourth band remains very small. For $\Delta = 8$, the band strongest affected is the second one, the population of the two highest bands remaining very small. Hence, the lowest band $\nu = 1$ is highest populated in the ground state and remains highest populated also after the excitation. Note that the distributions at $\Delta = 8$ are very flat, indicating localization in real space, while for $\Delta = 2$ some curvature is present, so that a stronger nonequilibrium dynamics can be expected, as indeed seen, e.g., in Fig. 10.

The question arises for how the MDF evolves in time. Due to the finite value of U^{HM} , we expect the electrons to scatter, so that the population of the four bands changes in time. In Figs. 17 and 18 we show the time evolution of the populations of each of the four bands with time for $\Delta = 2$ and $\Delta = 8$, respectively. Clearly, scattering between the bands takes place. However, it is difficult to draw a simple picture in which one could identify how the scattering from one band to the other happens in detail. What is apparent, is that for the larger value of Δ faster oscillations appear, and that the changes are much

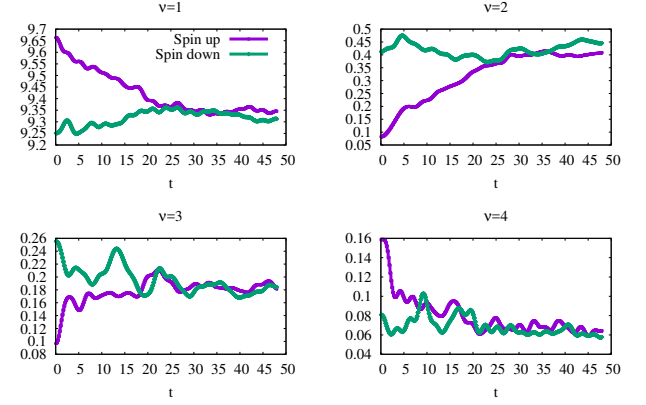


FIG. 17: tDMRG-results for the time evolution of the population of each band following the photoexcitation as in Fig. 15 for $\Delta = 2$.

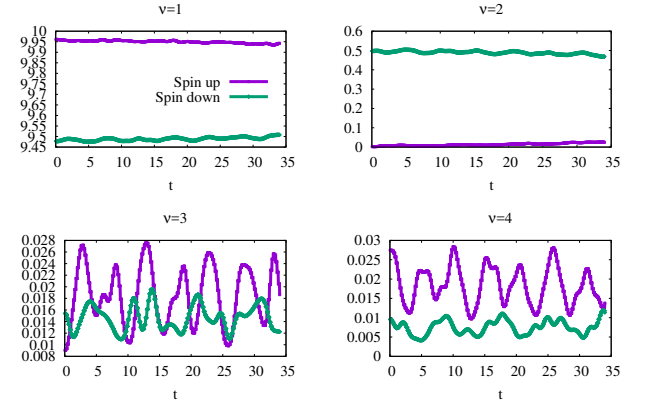


FIG. 18: tDMRG-results for the time evolution of the population of each band following the photoexcitation as in Fig. 16 for $\Delta = 8$.

smaller. Also, while for $\Delta = 2$ a clear trend for relaxation to a stationary state can be seen, on the time scales treated for $\Delta = 8$, indications for relaxing to a stationary state are rather weak. This again supports the picture that for large values of Δ the magnetic microstructure essentially traps the electrons so that scattering is inhibited, leading to a longer lifetime of the excitations.

The results discussed so far are obtained by exciting only a single site. Now, we turn to the more realistic case of a global excitation. Since the system sizes to get an initial state from the semiclassical treatment for the MPS-dynamics are too small to get significant insights, we consider excitations by applying operator Eq. (37) on every other site, emulating the main effect of the semiclassical excitation of polarizing each molecule. As expected, the change in the populations in each band are stronger, since we now are shifting not only one particle, but half of the population. The distributions look very similar to the ones shown in Figs. 15 and 16. In Figs. 19 and 20 we show the time evolution of these MDFs. As can

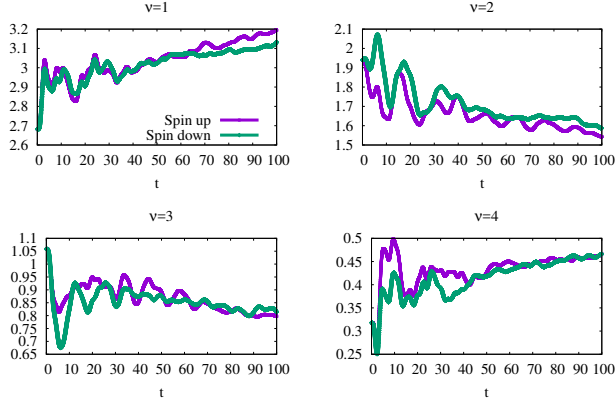


FIG. 19: tDMRG-results for the time evolution of the population of each band following the time evolution for $\Delta = 2$ after applying operator Eq. (37) at every other site of the system.

be seen, similar trends to the ones of Figs. 17 and 18 are obtained. However, due to symmetry of the spin sectors, we expect the evolution of the spin up and spin down sectors to be identical. This is realized at the beginning of the time evolution. At later times, differences become pronounced, while the main features remain. This difference we associate to the effect of the finite U^{HM} which is to scatter particles with different spins with each other.

III.4.2. Momentum distribution function of the quasiparticles

In Figs. 21 and 22 we show the quasiparticle distribution obtained from Eq. (47) at the beginning of the time evolution after applying operator Eq. (37) on each molecule. While we expect the quasiparticle picture to

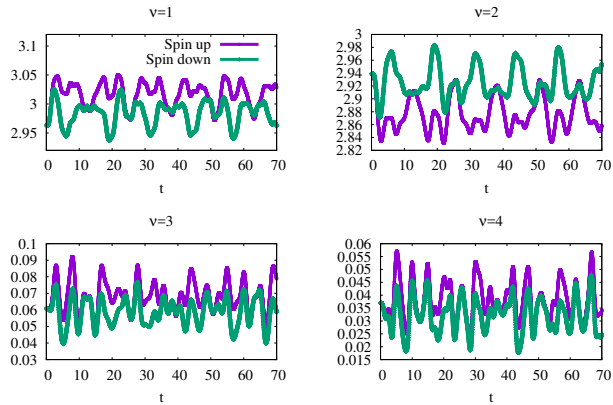


FIG. 20: tDMRG-results for the time evolution of the population of each band following the time evolution for $\Delta = 8$ after applying operator Eq. (37) at every other site of the system.

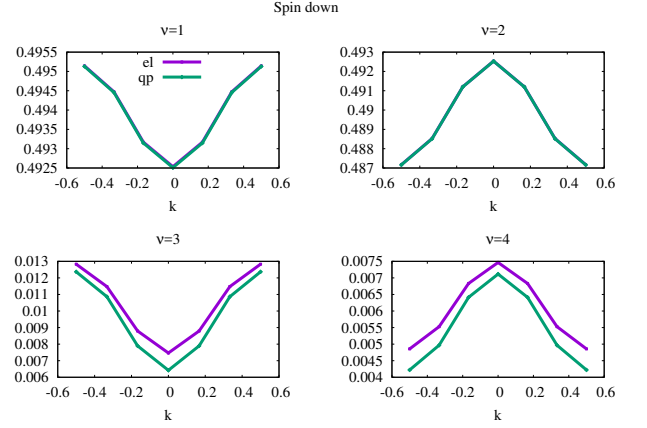


FIG. 21: Comparison of the electronic and the quasiparticle momentum distribution functions obtained with DMRG via Eq. (47) for a system with $L = 24$, $\Delta = 8$ and $U^{HM} = 3$ just after the photoexcitation by applying operator Eq. (37) at every other site of the system.

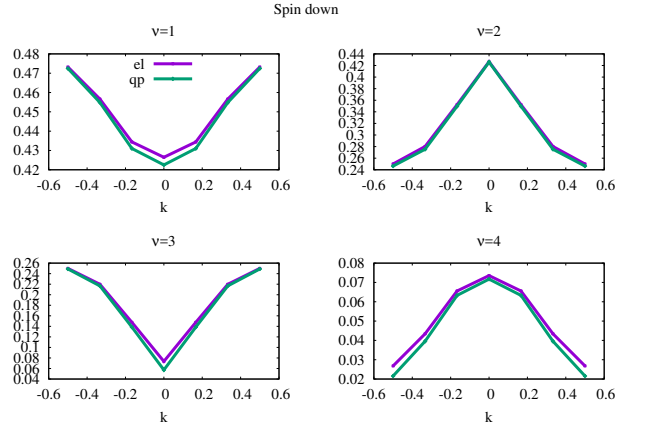


FIG. 22: Comparison of the electronic and the quasiparticle momentum distribution functions obtained with DMRG via Eq. (47) for a system with $L = 24$, $\Delta = 2$ and $U^{HM} = 3$ just after the photoexcitation by applying operator Eq. (37) at every other site of the system.

be better applicable at later times, it is nevertheless instructive to compare these electronic and quasiparticle distributions to each other. According to Eq. (47) we expect a renormalization by a k -dependent quasiparticle residue $Z(k)$ which is, however, constant in time, so that the time evolution of the QMD will be similar to the one of the electronic MDF, if the renormalization is not too strong. As can be seen, for both values of Δ shown, the renormalization of the electronic MDF is very small. The time evolution of the populations of the four bands as obtained from the QMD is therefore, up to a multiplicative constant close to one, identical to the evolution seen in Figs. 19 and 20.

III.5. Relaxation rates from Linearized Boltzmann Equations

With this picture in mind, we now estimate the lifetimes of the quasiparticles as described in Sec. II.7. We find the relaxation rates by diagonalizing the dimensionless linear operator $t_0(t_{hop}/U^{HM})^2 \hat{\mathcal{L}}[\phi]$ with the time scale $t_0 = \hbar/2\pi t_{hop} \approx 0.18$ fs. The result of our numerical evaluation is shown in Fig. 23. There we plot the results for a 2-band, a 3-band, and a 4-band calculation, where we always used the lowest bands possible. We can see that for final inverse temperature above $\beta \approx 1$, the calculations reveal the same relaxation rates, which means that the upper bands are not involved in the relaxation for low temperatures. Moreover for low temperature the relaxation rates decay exponentially in β , i.e.

$$\lambda_j \propto e^{-\Gamma_j \beta}. \quad (57)$$

For inverse temperatures larger than $\beta = 30$ the lowest eigenvalues are zero within numerical precision. Thus for low temperatures the corresponding contributions to the perturbation $\phi_\nu(k, t)$ become frozen.

The eigenvalues $n = 1, 2, 3$ depicted in Fig. 23 are zero numerically for every β . For the 3-band and 4-band calculation, there is an additional zero eigenvalue λ_+ , which we did not put in Fig. 23 for a better comparison of the other eigenvalues. We can explain these zero relaxation rates analytically. They correspond to the eigenfunctions

$$\begin{aligned} (\chi_\nu^{(1)}(k))_{\nu=1,\dots,4} &= (1, 1, 1, 1) \forall k, \\ (\chi_\nu^{(2)}(k))_{\nu=1,\dots,4} &= (\omega_1(k), \omega_2(k), \omega_3(k), \omega_4(k)) \forall k, \\ (\chi_\nu^{(3)}(k))_{\nu=1,\dots,4} &= (1, 0, 1, 0) \forall k, \\ (\chi_\nu^{(+)}(k))_{\nu=1,\dots,4} &= (1, 1, 0, 0) \forall k. \end{aligned} \quad (58)$$

Since $\hat{\mathcal{L}}$ is linear all combination of these eigenfunctions are conserved. They correspond to quantum-mechanical state space operators of the form $\hat{\Phi}[\psi] = \int dk \psi_\nu(k) n_\nu^{\text{qp}}(k)$:

$$\begin{aligned} \hat{\Phi}[\chi^{(1)}] &= \hat{N} \quad (\text{total number of particles}), \\ \hat{\Phi}[\chi^{(2)}] &= \hat{H} + \mathcal{O}(U) \quad (\text{total energy}), \\ \hat{\Phi}[\chi^{(3)}] &= \hat{N}_1 + \hat{N}_3, \\ \hat{\Phi}[\chi^{(+)}] &= \hat{N}_1 + \hat{N}_2, \end{aligned} \quad (59)$$

with the band number operators $\hat{N}_\nu = \int dk n_\nu^{\text{qp}}(k)$. Hence a contribution of $\chi_\nu^{(1)}(k)$ to the perturbation $\phi_\nu(k, t)$ leads to a change of the total number of particles $\langle \hat{N} \rangle$, i.e. a change of the chemical potential μ . A contribution of $\chi_\nu^{(2)}(k)$ changes the total temperature. A contribution of either of them means that the thermal distribution $f_\nu(k)$, which we used for the linearization, was not calculated correctly in the first place, but the final temperature and the final chemical potential are different.

The eigenfunction $\chi_\nu^{(3)}(k)$ mean that the number of particles in the first plus those in the third band cannot be changed during the relaxation process. Similarly $\chi_\nu^{(+)}(k)$ is related to the conservation of particles in the first plus the second band. Obviously this eigenfunction is the same as $\chi_\nu^{(1)}(k)$, if we do not include the bands 3 and 4. This is the reason for the additional zero eigenvalue λ_+ in the 3- and 4-band case. A contribution from either of the eigenfunctions $\chi_\nu^{(3)}(k)$ and $\chi_\nu^{(+)}(k)$ leads to at least two different chemical potentials in the long time limit. The cause of this is the relatively large value of Δ . Therefore, the gaps between the bands are so large that some of the two-particle scattering processes are forbidden by energy conservation.

We conclude that the system relaxes on long time scales beyond the reach of tDMRG to thermal distributions with separate chemical potentials for the different bands. The relaxation rates depend very sensitively on the final temperature and thereby the energy density of the photoexcitation. This would be a clear experimental signature of a purely electron-electron interaction driven thermalization dynamics in one dimension.

IV. CONCLUSIONS AND SUMMARY

To summarize, by combining tight-binding models derived from ab-initio methods, MPS techniques, and quantum Boltzmann equation approaches we have elucidated the photoexcitation dynamics in 1D model manganite systems over a wide span of time scales. We develop a Hubbard-type model which allows to take into account the effect of strong correlations on the dynamics. For the photoexcitation, we introduce a semiclassical approach which takes into account the back-action of the electrons to the light-field. The subsequent time evolution shows that the lifetime of the excitations is enhanced by the presence of magnetic microstructures. The lifetime of excitations is then estimated by a linearized Boltzmann equation approach.

A tight-binding model for the one-dimensional manganite treated here has been derived from a tight-binding model which was developed for three dimensional $\text{Pr}_{1-x}\text{Ca}_x\text{MnO}_3$, capturing the entire range of doping. This three dimensional model has been determined in a joint effort using experimental methods and first-principles calculations.³¹ The tight-binding model describes electron, spin, and phonon degrees of freedom which interact strongly by electron-electron, electron-spin and electron-phonon interactions. The electronic subsystem is described by a single Slater determinant as in density functional theory. Coulomb and screened exchange are taken into account, so that both the limit of weakly and of strongly interacting electrons can be described. The description of the electrons is based on the Pauli equation, which provides an intrinsically non-collinear description of the magnetization. The spins are described by a classical Heisenberg model and the phonons are described as distortions of classical parti-

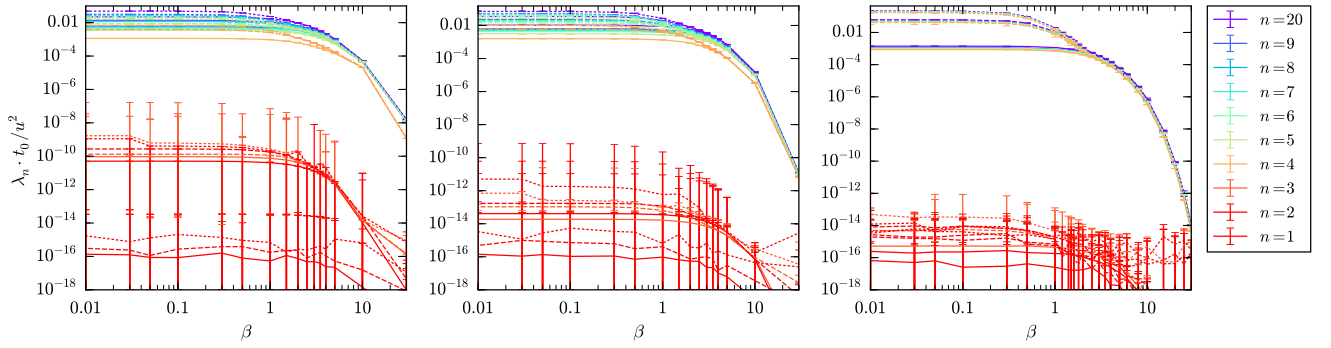


FIG. 23: Relaxation rates as obtained from the linearized Boltzmann equation approach for $\Delta = 1, 2, 4$ from left to right. The eigenvalues λ_n of $\hat{\mathcal{L}}$ are sorted by their magnitude and we plot the lowest ones ($n = 1, 2, 3, \dots$) as function of inverse temperature β . In all of the plots, the full lines are calculations with the lowest two bands, the dashed lines indicate a calculation with the three lowest bands, and the dotted lines denote a computation with all the four bands. The eigenvalues $n = 1, 2, 3$ are zero within numerical precision. Note that for the 3- and 4-band calculation there is an additional zero eigenvalue, which we omitted in the legend for comparability. As an example for a relaxation time, we consider $u = U^{HM}/t_{hop} = 3$ at room temperature $\beta = t_{hop}/(k_B \cdot 300 \text{ K}) \approx 23$. With $\Delta = 2$, and $t_{hop} \approx 0.585 \text{ eV}$, and $t_0 := \hbar/\pi t_{hop} \approx 0.36 \text{ fs}$ the smallest relaxation time is $1/\lambda_4 = 10^9 t_0 / u^2 \approx 40 \text{ ns}$.

cles.

The tight-binding model has been used to explore the phase space of the one-dimensional model manganites for various doping. In a coarse graining approach a polaron model has been extracted from the tight-binding calculations. The types of polarons detected are electron-, Zener-, hole-, and Jahn-Teller-polarons, i.e., the main classes of polarons observed in 3d manganites are captured. Hence, the low-energy scale of 1-d manganites can well be described in terms of polarons as basic entities, their reactions and interactions. The underlying physical mechanism leading to the different polarons is described. Using the polaron picture, the zero-temperature phases are readily rationalized. In this way, our findings provide a blueprint for a description of physical manganites at higher dimensions.

Of particular interest for us is the situation at half doping. Here, the ground state is formed by a lattice of Zener polarons which are dimers of two ferromagnetically aligned Mn-sites, which show a certain analogy to a hydrogen molecule. The Zener polarons are coupled antiferromagnetically among each other. This finding we use as a starting point to write down a one-dimensional Hubbard-type strongly interacting model which takes into account the dimerization found in this lattice of Zener polarons by adding an alternating dimerized magnetic field to the usual Hubbard model.

Based on this, we formulate our semiclassical approach for modeling the photoexcitation. It allows us to include in a natural way the back action of the electrons to the incoming light-field during the photoexcitation process. In comparison to the frequently used Peierls substitution ansatz in which the photons are treated as classical external electromagnetic field, due to the inclusion of the back action of the electrons to the light-field, the resulting polarization of the system is stronger. This finding

needs to be further explored in future studies, as well as possibilities to extend the semiclassical ansatz to situations beyond 1D and for further systems. In the situations studied here, the result of this treatment is that the photo-excitation - essentially - shifts one electron on every other lattice site, so that a nearly fully polarized state is obtained. This can also be realized by directly implementing such an excitation in the tDMRG, allowing us to reach larger system sizes.

The short-time dynamics of the photoexcitation is then studied using the tDMRG. This reveals that the presence of the staggered magnetic field in our Hubbard-type model, i.e., the magnetic microstructure caused by the Zener polarons, strongly influences the time scales of the dynamics and hence the lifetimes of the excitations. While for very small values of the magnetic field the excitation very quickly dies out (at zero field this would happen on a time scale $\sim 10 \text{ fs}$), for large values of the magnetic field the dynamics resembles localized excitons which are trapped by the microstructure. This is interesting, and further possible relations to experimental findings need to be explored. The tDMRG results for the momentum distribution function clearly show that scattering leads to a redistribution of the electrons on the four bands of the system. Estimating the quasiparticle content from the electronic momentum distribution functions reveals that only a small, time independent renormalization is realized, so that the time evolution of the quasiparticle momentum distribution is very similar to the one of the electrons.

Having this in mind, we apply a linearized Boltzmann equation ansatz for estimating the lifetimes of the excitations. For the long-time dynamics, it predicts evolution to thermal distributions with separate chemical potentials for the different bands. This thermalization already follows from electron-electron interactions in this one di-

mensional system, similar to the results in Ref. 43 for the one-dimensional Hubbard model. The thermalization rates in our PCMO model are always exponentially suppressed as a function of the inverse final temperature (this is different from Ref. 43), which would be a clear experimental signature if initially the sample is at sufficiently low temperature. This exponential suppression is a specific consequence of the one dimensional nature of our PCMO model. However, it should be noted that depending on the strength of the electron-phonon coupling this signature might be hidden by coupling to the phonon bath. Realistic modeling and inclusion of the phonon degrees of freedom is left to future work.

ACKNOWLEDGMENTS

We acknowledge fruitful discussions with Z. Lenarčič, F. Heidrich-Meisner, and E. Jeckelmann. Financial support from the Deutsche Forschungsgemeinschaft (DFG) through SFB/CRC1073 (Projects B03 and C03) is gratefully acknowledged. S.R.M. acknowledges hospitality of the Kavli Institute for Theoretical Physics (KITP), Santa Barbara, where part of this research was accomplished and supported in part by the NSF under Grant No. NSF PHY11-25915. We acknowledge numerous insightful discussions with Thomas Pruschke (deceased). S.R. and P.B. thank Robert Schade for his help with the tight-binding code. P.B. thanks Christian Jooss for numerous discussions on the manganites.

Appendix A: Boltzmann equation for electron relaxation

Based on the effective model from Sec. II.2.3, Eq. (21), we can investigate the relaxation of the electrons due to electron-electron interactions by means of a BE. We use it in a similar manner as Biebl and Kehrein⁴³, who investigated the thermalization rates of a Hubbard model. Furthermore we perform a linearization of the BE to find the relaxation rates.

1. Multi-band Boltzmann equation

To investigate the relaxation of the QMD $n_{\sigma\nu}(k, t)$ we use the multi-band BE

$$\dot{n}_{\sigma\nu}(k, t) = \mathcal{I}_{\text{coll}}[n]_{\sigma\nu}(k, t). \quad (\text{A1})$$

We assume in the following that the spin \uparrow particles have the same QMD as those with spin \downarrow . Hence we can drop the spin degree of freedom σ , i.e. $n_{\sigma\nu}(k, t) = n_{\nu}(k, t)$.

Thus the collision term is

$$\begin{aligned} \mathcal{I}_{\text{coll}}[n]_1 &= \frac{\pi U^2}{\hbar t_{\text{hop}}} \int_{\mathbb{K}^3} dk_2 dk_3 dk_4 \sum_{\substack{G \in \mathbb{Z}, \\ \nu_{2,3,4} \in \mathbb{B}}} |\Phi_{\vec{\nu}, \vec{k}}|^2 \delta(P_{\vec{k}} + G) \delta(W_{\vec{\nu}, \vec{k}}) \\ &\times |\Phi_{\vec{\nu}, \vec{k}}|^2 \left\{ \underbrace{(1-n_1)(1-n_2)n_3n_4}_{\text{gain term}} - \underbrace{n_1n_2(1-n_3)(1-n_4)}_{\text{loss term}} \right\}, \end{aligned} \quad (\text{A2})$$

where we introduced the abbreviation $X_j := X_{\nu_j}(k_j, t)$ and the set $\mathbb{B} = \{1, 2, 3, 4\}$ containing the band numbers. We defined $\Phi_{\vec{\nu}, \vec{k}}$ as the matrix element of the interaction taken at four momenta in four bands. Moreover $W_{\vec{\nu}, \vec{k}} = \omega_1 + \omega_2 - \omega_3 - \omega_4$ is the energy shift and $P_{\vec{k}} + G = (k_1 + k_2 - k_3 - k_4) + G$ the momentum difference of the respective scattering process taking into account Umklapp processes by the reciprocal lattice vector $G \in \mathbb{Z}$. The collision integral of a model describing an infinite lattice naturally allows for Umklapp processes. We account for this by integrating k_4 over a larger scope than only the first Brillouin zone. We want to emphasize that this is an exact reformulation of the derived collision integral.

A first step towards calculating the BE is finding the single particle bands $\omega_{\nu}(k)$ which we obtain from diagonalizing \hat{H}_0 , see Eq. (27). To do this we rewrite it such that the unit cells containing the 4 sites are revealed. Hence we introduce the index $l \in \mathbb{Z}$ labeling the unit-cells and $j \in \mathbb{B}$ labeling the four sites within the unit cell and find:

$$\hat{H}_0 = \sum_{\sigma l j j'} \left[\mathcal{A}_{\sigma j j'} \hat{c}_{\sigma l j}^\dagger \hat{c}_{\sigma l j'} + \left(\mathcal{B}_{j j'} \hat{c}_{\sigma l j}^\dagger \hat{c}_{\sigma l+1, j} + H.c. \right) \right] \quad (\text{A3})$$

with

$$\begin{aligned} \mathcal{A}_{\uparrow} &:= \begin{bmatrix} E_1 & -t_{\text{hop}} & 0 & 0 \\ -t_{\text{hop}} & E_2 & -t_{\text{hop}} & 0 \\ 0 & -t_{\text{hop}} & E_2 & -t_{\text{hop}} \\ 0 & 0 & -t_{\text{hop}} & E_1 \end{bmatrix}, \\ \mathcal{A}_{\downarrow} &:= \begin{bmatrix} E_2 & -t_{\text{hop}} & 0 & 0 \\ -t_{\text{hop}} & E_1 & -t_{\text{hop}} & 0 \\ 0 & -t_{\text{hop}} & E_1 & -t_{\text{hop}} \\ 0 & 0 & -t_{\text{hop}} & E_2 \end{bmatrix}, \end{aligned} \quad (\text{A4})$$

and

$$\mathcal{B} := \begin{bmatrix} 0 & 0 & 0 & 0 \\ 0 & 0 & 0 & 0 \\ 0 & 0 & 0 & 0 \\ -t_{\text{hop}} & 0 & 0 & 0 \end{bmatrix}. \quad (\text{A5})$$

Since the unit cell repeats itself it is useful to apply a Fourier-transform to the unit-cell index l :

$$\hat{c}_{\sigma l j} = \int dk e^{i2\pi k l} \hat{b}_{\sigma j}(k). \quad (\text{A6})$$

This leads to

$$\hat{H}_0 = \sum_{\sigma jj'} \int dk \hat{b}_{\sigma j}^\dagger(k) \hat{b}_{\sigma j'}(k) \underbrace{\left[\mathcal{A}_{\sigma jj'} + \mathcal{B}_{jj'} e^{ik} + \mathcal{B}_{jj'}^\dagger e^{-ik} \right]}_{=: \mathcal{C}_{\sigma jj'}(k)}. \quad (\text{A7})$$

We only have to diagonalize the 4-by-4 matrix $\mathcal{C}_\sigma(k)$ using the unitary transformation $T_{\sigma j\nu}(k)$:

$$\begin{aligned} T_\sigma^\dagger(k) \mathcal{C}_\sigma(k) T_\sigma(k) &= \mathcal{D}_\sigma(k), \\ \mathcal{D}_{\sigma\nu\nu'}(k) &= t_{hop} \delta_{\nu\nu'} \omega_{\sigma\nu}(k), \end{aligned} \quad (\text{A8})$$

where

$$\omega_\nu(k) = \pm \frac{1}{2} \sqrt{8 + \Delta^2 \pm 4\sqrt{2(1 + \cos(2\pi k)) + \Delta^2}}. \quad (\text{A9})$$

Thus

$$\hat{H}_0 = t_{hop} \sum_{\sigma jj'\nu} \int dk \hat{b}_{\sigma j}^\dagger(k) \hat{b}_{\sigma j'}(k) T_{\sigma j\nu}(k) \omega_{\sigma\nu}(k) T_{\sigma j'\nu}^*(k). \quad (\text{A10})$$

We get rid of the two transformation matrices by transforming the creation and annihilation operators:

$$\hat{a}_{\sigma\nu}(k) = \sum_{j \in \mathbb{B}} T_{\sigma j\nu}(k) \hat{b}_{\sigma j}(k). \quad (\text{A11})$$

We finally obtain

$$\hat{H}_0 = t_{hop} \sum_{\sigma \in \mathbb{S}} \sum_{\nu \in \mathbb{B}} \int dk \omega_\nu(k) \hat{n}_{\sigma\nu}(k) \quad (\text{A12})$$

with the number operator $\hat{n}_{\sigma\nu}(k) = \hat{a}_{\sigma\nu}^\dagger(k) \hat{a}_{\sigma\nu}(k)$. We see that $\omega_\nu(k)$ are the four single-particle bands.

Note that the bands do not depend on the spin σ , because for the single particle Hamiltonian the states of spin \uparrow are the same as those for spin \downarrow . The only difference is that they are shifted by two sites. Hence the transformation $T_{\sigma i\nu}(k)$ can be chosen such that the bands do not depend on the spin. However, the choice of the transformation affects the interaction part of the Hamiltonian, which is

$$\begin{aligned} \hat{H}_{\text{int}} &= U \sum_{\vec{\nu} \in \mathbb{B}^4} \int d^4k \delta(P_{\vec{k}}) \Phi_{\vec{\nu}, \vec{k}} \\ &\quad \times \hat{a}_{\uparrow\nu_1}^\dagger(k_1) \hat{a}_{\downarrow\nu_2}^\dagger(k_2) \hat{a}_{\downarrow\nu_3}(k_3) \hat{a}_{\uparrow\nu_4}(k_4). \end{aligned} \quad (\text{A13})$$

Hereby the matrix elements are

$$\Phi_{\vec{\nu}, \vec{k}} = \sum_{i \in \mathbb{Z}} T_{\uparrow i, \nu_1}^*(k_1) T_{\downarrow i, \nu_2}^*(k_2) T_{\downarrow i, \nu_3}(k_3) T_{\uparrow i, \nu_4}(k_4). \quad (\text{A14})$$

-
- ¹ M. Rini, R. Tobey, N. Dean, J. Itatani, Y. Tomioka, Y. Tokura, R. W. Schoenlein, and A. Cavalleri, *Nature* **449**, 72 (2007).
 - ² I. Avigo, S. Thirupathaiah, M. Ligges, T. Wolf, J. Fink, and U. Bovensiepen, *New Journal of Physics* **18**, 093028 (2016).
 - ³ F. Schmitt, P. S. Kirchmann, U. Bovensiepen, R. G. Moore, L. Rettig, M. Krenz, J.-H. Chu, N. Ru, L. Perfetti, D. H. Lu, M. Wolf, I. R. Fisher, and Z.-X. Shen, *Science* **321**, 1649 (2008), <http://science.sciencemag.org/content/321/5896/1649.full.pdf>.
 - ⁴ Z. Tao, C. Chen, T. Szilvási, M. Keller, M. Mavrikakis, H. Kapteyn, and M. Murnane, *Science* **353**, 62 (2016), <http://science.sciencemag.org/content/353/6294/62.full.pdf>.
 - ⁵ M. Mitrano, A. Cantaluppi, D. Nicoletti, S. Kaiser, A. Perucchi, S. Lupi, P. Di Pietro, D. Pontiroli, M. Riccò, S. R. Clark, D. Jaksch, and A. Cavalleri, *Nature* **530**, 461 (2016), letter.
 - ⁶ W. Hu, S. Kaiser, D. Nicoletti, C. R. Hunt, I. Gierz, M. C. Hoffmann, M. Le Tacon, T. Loew, B. Keimer, and A. Cavalleri, *Nat Mater* **13**, 705 (2014), article.
 - ⁷ Z. Lenarčič and P. Prelovšek, *Phys. Rev. Lett.* **111**, 016401 (2013).
 - ⁸ Z. Lenarčič, M. Eckstein, and P. Prelovšek, *Phys. Rev. B* **92**, 201104 (2015).
 - ⁹ M. Eckstein and P. Werner, *Physical review letters* **110**, 126401 (2013).
 - ¹⁰ P. Werner and M. Eckstein, *Structural Dynamics* **3**, 023603 (2016), <http://dx.doi.org/10.1063/1.4935245>.
 - ¹¹ D. Fausti, R. I. Tobey, N. Dean, S. Kaiser, A. Dienst, M. C. Hoffmann, S. Pyon, T. Takayama, H. Takagi, and A. Cavalleri, *Science* **331**, 189 (2011), <http://science.sciencemag.org/content/331/6014/189.full.pdf>.
 - ¹² K. Zhao, Y.-H. Huang, H.-B. Lü, M. He, K.-J. Jin, Z.-H. Chen, Y.-L. Zhou, B.-L. Cheng, S.-Y. Dai, and G.-Z. Yang, *Chinese Physics* **14**, 420 (2005).
 - ¹³ K. Zhao, K.-j. Jin, H. Lu, Y. Huang, Q. Zhou, M. He, Z. Chen, Y. Zhou, and G. Yang, *Applied Physics Letters* **88**, 141914 (2006).
 - ¹⁴ H. Ni, Z. Yue, K. Zhao, W. Xiang, S. Zhao, A. Wang, Y.-C. Kong, and H.-K. Wong, *Opt. Express* **20**, A406 (2012).
 - ¹⁵ H. J. Snaith, *The Journal of Physical Chemistry Letters* **4**, 3623 (2013), <http://dx.doi.org/10.1021/jz4020162>.
 - ¹⁶ J. Gong, S. B. Darling, and F. You, *Energy Environ. Sci.* **8**, 1953 (2015).
 - ¹⁷ G. Saucke, J. Norpoth, C. Jooss, D. Su, and Y. Zhu, *Phys. Rev. B - Condens. Matter Mater. Phys.* **85**, 1 (2012).
 - ¹⁸ B. Iffland, P. Peretzki, B. Kressdorf, P. Saring, A. Kelling, M. Seibt, and C. Jooss, *Beilstein J. Nanotechnol.* **6**, 1467 (2015).
 - ¹⁹ R. P. Prasankumar, S. Zvyagin, K. V. Kamenev, G. Balakrishnan, D. M. Paul, A. J. Taylor, and R. D. Averitt, *Phys. Rev. B* **76**, 020402 (2007).
 - ²⁰ J. Bielecki, R. Rauer, E. Zanghellini, R. Gunnarsson, K. Dörr, and L. Börjesson, *Phys. Rev. B* **81**, 064434 (2010), [arXiv:1002.4828 \[cond-mat.str-el\]](https://arxiv.org/abs/1002.4828).
 - ²¹ R. E. Peierls, *Z. Phys.* **80**, 763 (1933).
 - ²² M. Graf and P. Vogl, *Phys. Rev. B* **51**, 4940 (1995).
 - ²³ D. R. Hofstadter, *Phys. Rev. B* **14**, 2239 (1976).
 - ²⁴ K. Jiménez-García, L. J. LeBlanc, R. A. Williams, M. C. Beeler, A. R. Perry, and I. B. Spielman, *Phys. Rev. Lett.* **108**, 225303 (2012).
 - ²⁵ W. Shen, Y. Ge, A. Y. Liu, H. R. Krishnamurthy, T. P. Devereaux, and J. K. Freericks, *Phys. Rev. Lett.* **112**, 176404 (2014).
 - ²⁶ L. G. D. da Silva, K. A. Al-Hassanieh, A. E. Feiguin, F. A.

- Reboredo, and E. Dagotto, *Physical Review B* **81**, 125113 (2010).
- ²⁷ F. Hofmann and M. Potthoff, *Phys. Rev. B* **85**, 205127 (2012).
- ²⁸ S. Wall, D. Brida, S. R. Clark, H. P. Ehrke, D. Jaksch, A. Ardavan, S. Bonora, H. Uemura, Y. Takahashi, T. Hasegawa, *et al.*, *Nature Physics* **7**, 114 (2011).
- ²⁹ K. A. Al-Hassanieh, F. A. Reboredo, A. E. Feiguin, I. González, and E. Dagotto, *Phys. Rev. Lett.* **100**, 1 (2008), [arXiv:0804.0617](#).
- ³⁰ V. Markovich, A. Wisniewski, and H. Szymczak, in *Handbook of Magnetic Materials*, Handbook of Magnetic Materials, Vol. 22, edited by K. Buschow (Elsevier, 2014) pp. 1–201.
- ³¹ M. Sotoudeh, S. Rajpurohit, P. Blöchl, D. Mierwaldt, J. Norpoth, V. Roddatis, S. Mildner, B. Ifland, and C. Jooss, in preparation (2016).
- ³² E. Perfetto, D. Sangalli, A. Marini, and G. Stefanucci, *Phys. Rev. B* **92**, 205304 (2015).
- ³³ S. R. White, *Phys. Rev. Lett.* **69**, 2863 (1992).
- ³⁴ S. R. White, *Phys. Rev. B* **48**, 10345 (1993).
- ³⁵ U. Schollwöck, *Rev. Mod. Phys.* **77**, 259 (2005).
- ³⁶ A. J. Daley, C. Kollath, U. Schollwöck, and G. Vidal, *J. Stat. Mech.: Theor. Exp.*, P04005 (2004).
- ³⁷ S. R. White and A. E. Feiguin, *Phys. Rev. Lett.* **93**, 076401 (2004).
- ³⁸ A. J. Daley, *Advances in Physics* **63**, 77 (2014).
- ³⁹ U. Schollwöck, *Annals of Physics* **326**, 96 (2011).
- ⁴⁰ J. Haegeman, J. I. Cirac, T. J. Osborne, I. Pižorn, H. Verschelde, and F. Verstraete, *Phys. Rev. Lett.* **107**, 070601 (2011).
- ⁴¹ J. Haegeman, C. Lubich, I. Oseledets, B. Vandereycken, and F. Verstraete, *ArXiv e-prints* (2014), [arXiv:1408.5056 \[quant-ph\]](#).
- ⁴² F. H. L. Essler, S. Kehrein, S. R. Manmana, and N. J. Robinson, *Phys. Rev. B* **89**, 165104 (2014).
- ⁴³ F. R. A. Biebl and S. Kehrein, *ArXiv e-prints* (2016), [arXiv:1607.07115 \[cond-mat.stat-mech\]](#).
- ⁴⁴ E. Dagotto, *Nanoscale Phase Separation and Colossal Magnetoresistance* (Springer, 2003).
- ⁴⁵ G. Jonker and J. V. Santen, *Physica* **16**, 337 (1950).
- ⁴⁶ E. O. Wollan and W. C. Koehler, *Phys. Rev.* **100**, 545 (1955).
- ⁴⁷ T. Hotta, *Rep. Prog. Phys.* **69**, 2061 (2006).
- ⁴⁸ P. Hohenberg and W. Kohn, *Phys. Rev.* **136**, B864 (1964).
- ⁴⁹ W. Kohn and L. J. Sham, *Phys. Rev.* **140**, A1133 (1965).
- ⁵⁰ P. E. Blöchl, *Phys. Rev. B* **50**, 17953 (1994).
- ⁵¹ P. Blöchl, unpublished (2016).
- ⁵² U. Schollwöck, *Annals of Physics* **326**, 96 (2011), january 2011 Special Issue.
- ⁵³ L. G. G. V. Dias da Silva, K. A. Al-Hassanieh, A. E. Feiguin, F. A. Reboredo, and E. Dagotto, *Phys. Rev. B* **81** (2010), [10.1103/physrevb.81.125113](#).
- ⁵⁴ Z. Lenarčič and P. Prelovšek, *Phys. Rev. B* **90**, 235136 (2014).
- ⁵⁵ N. ten Brinke, M. Ligges, U. Bovensiepen, and R. Schützhold, *ArXiv e-prints* (2016), [arXiv:1602.00871 \[quant-ph\]](#).
- ⁵⁶ J. H. Mentink, K. Balzer, and M. Eckstein, *Nature Communications* **6**, 6708 EP (2015), article.
- ⁵⁷ M. Eckstein and P. Werner, *Phys. Rev. B* **88**, 075135 (2013).
- ⁵⁸ F. Dorfner, L. Vidmar, C. Brockett, E. Jeckelmann, and F. Heidrich-Meisner, *Phys. Rev. B* **91**, 104302 (2015).
- ⁵⁹ C. Brockett, F. Dorfner, L. Vidmar, F. Heidrich-Meisner, and E. Jeckelmann, *Phys. Rev. B* **92**, 241106 (2015).
- ⁶⁰ S. C. Kramer, *CUDA-based Scientific Computing: Tools and Selected Applications* (Niedersächsische Staats- und Universitätsbibliothek Göttingen, 2013).
- ⁶¹ cuBLAS is an implementation of BLAS library especially for the usage on nVidia CUDA devices.
- ⁶² M. Moeckel and S. Kehrein, *Phys. Rev. Lett.* **100**, 175702 (2008).
- ⁶³ H. Haug and A.-P. Jauho, *Quantum Kinetics in Transport and Optics of Semiconductors* (Springer, 1996).
- ⁶⁴ R. Car and M. Parrinello, *Phys. Rev. Lett.* **55**, 2471 (1985).
- ⁶⁵ E. Perfetto, A.-M. Uimonen, R. van Leeuwen, and G. Stefanucci, *Phys. Rev. A* **92**, 033419 (2015).
- ⁶⁶ F. H. L. Essler, H. Frahm, F. Göhmann, A. Klümper, and V. E. Korepin, *The One-Dimensional Hubbard Model* (Cambridge University Press, Cambridge, 2005).
- ⁶⁷ P. Calabrese and J. Cardy, *Phys. Rev. Lett.* **96**, 136801 (2006).
- ⁶⁸ S. R. Manmana, S. Wessel, R. M. Noack, and A. Muramatsu, *Phys. Rev. B* **79**, 155104 (2009).
- ⁶⁹ M. Cheneau, P. Barmettler, D. Poletti, M. Endres, P. Schauß, T. Fukuhara, C. Gross, I. Bloch, C. Kollath, and S. Kuhr, *Nature* **481**, 484 (2012).